From Top to Bottom - the Multiwavelength Campaign of V824 Ara (HD 155555)

Robert Dempsey[1], James Neff[2] Klaus Strassmeier[3], Jeffrey Linsky[4], Jeremy Lim[5], J-F. Donati[6], Fred Walter[2], Edwin Budding[7], Fred Marang[8], Ian Jordan[9], Stan Walker[9], David G. Downing[9], Doug Inwood[9], Orlon Petterson[9]

1. Introduction

A great deal of progress has been made in recent years in decomposing the 2-D structure in the atmospheres of late-type stars. Doppler images of many photospheres - single stars, T Tauri stars, Algols, RS CVn binaries to name a few - are regularly published (Strassmeier 1996; Richards & Albright 1996; Rice & Strassmeier 1996; Kürster et al. 1994). Ultraviolet spectral images of chromospheres appear in the literature (e.g., Walter et al. 1987; Neff et al. 1989) but are less common owing to the difficult nature of obtaining complete phase coverage. Zeeman doppler images of magnetic fields are now feasible (e.g., Donati et al. 1992). Performing Doppler imaging of the same targets over many seasons has also been accomplished (e.g, Vogt et al. 1997). Even when a true image reconstruction is not possible due to poor spectral resolution, we can still infer a great deal about spatial structure if enough phases are observed. However, it is increasingly apparent that to make sense of recent results, many different spectral features spanning a range of formation temperature and density must be observed *simultaneously* for a coherent picture to emerge.

Here we report on one such campaign. In 1996, we observed the southern hemisphere RS CVn binary V824 Ara ($P=1^d.68$, G5IV+K0V-IV) over one complete stellar rotation with the Hubble Space Telescope and EUVE. In conjunction, radio and optical photometry and spectroscopy were obtained from the ground. Unique to this campaign is the complete phase coverage of a number

[1] Space Telescope Science Institute

[2] State University of New York, Stony Brook

[3] University of Vienna

[4] Joint Institute for Laboratory Astrophysics

[5] Center for Astrophysics and Space Astronomy

[6] Observatoire de Meudon

[7] Central Institute of Technology

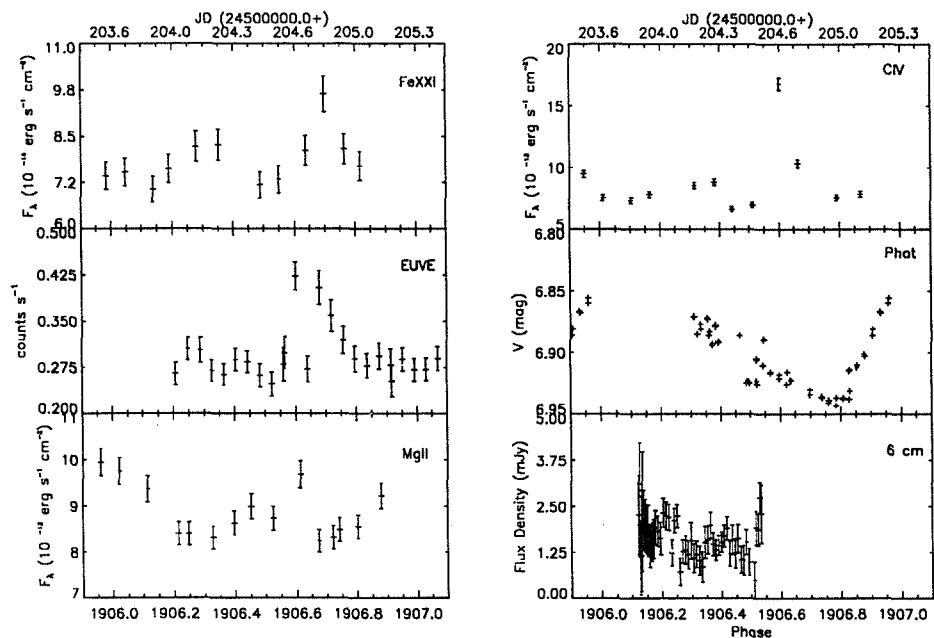[8] South African Astronomical Observatory

[9] New Zealand

Figure 1. Extracted light curves for observations obtained simultaneously with those of HST, except for the photometric data. The displayed photometry is a folded light curve obtained from before, during, and after the HST data but little evolution is observed. Phases are computed according to the orbit computed by Pasquini et al. (1991) and phase 1906.25 corresponds to conjunction with the K star in front.

of activity proxy indicators that cover source temperatures ranging from the photosphere to the corona.

2. Observations

Extracted light curves for the interval centered on the HST observations (except for the photometry) is given in Fig. 1. A flare event is observed near phase $\phi = 1906.6$ (Fig. 2). During the observing campaign the following observations were obtained:

- **HST** - In all, some 48,000 spectra were obtained with the Goddard High Resolution Spectrograph (GHRS), mostly centered on the 1354 Å region in RAPID ($\sim$ 1 second exposure) mode. The 1354 Å spectral region contains the Fe XXI emission line which has been identified by Maran et al. (1994) as coronal in nature ($T \sim 10^7$K). All rapid readout spectra were analyzed individually to search for flares and then summed into 11 spectra. One high resolution, high S/N ACCUM spectra was also obtained of the 1354 Å region for comparison. See Fig. 3. Spectra covering the Mg II h- and k-lines and the C IV doublet were obtained at 15 and 12 phases, respectively, in ACCUM mode.
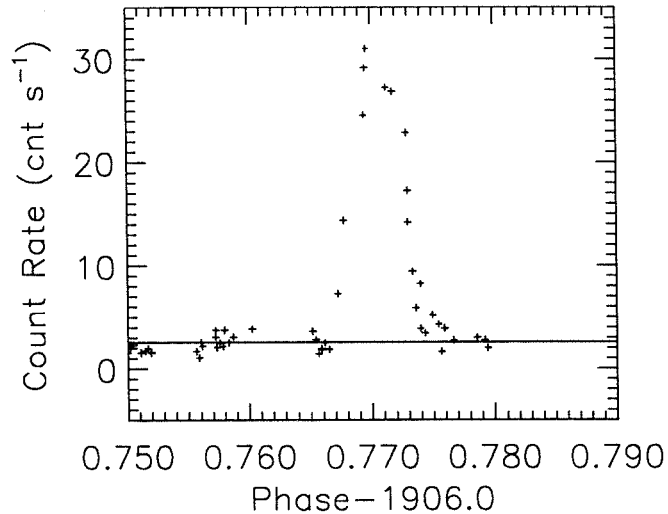
2

Figure 2. Count rate in the Fe XXI spectrum (entire range) as a function of phase. The dark count rate, based on theoretical models computed as a function of latitude and longitude, has been removed. The solid line indicates the mean level obtained outside of the flare.

- **EUVE** - V824 Ara was observed by EUVE for 44ksec simultaneously with the HST using the Short (SW), Medium (MW), Long (LW) wavelength, and DS detectors. Due to the (shortened) exposure time, only the Fe XVIII (93.93 Å) and Fe XXIII+Fe XX (132.8 Å) features were reliably detected, although other transitions may be marginally measurable.

- **CTIO** - Optical spectroscopy for Doppler imaging was obtained with the 1.5m telescope using a 2048x2048 chip in echelle mode. Each observation covered the He I (D3), Na I (D), Ca I (6439 Å), Fe I (6546 Å), Hα, Fe I (6663 Å), Li I (6707 Å), Ca I (6717 Å), and TiO (7055 Å) absorption features.

- **AT** - Observations at 3 and 6 cm were obtained with the Australian Telescope over a 5 day period when the target was visible from the ground.

- **Photometry** - Optical Johnson photometry were obtained at three sites, using either single-channel photometers or CCDs.

- **ESO** - Optical spectroscopy for Doppler imaging was also obtained with the ESO 1.4m CAT/CES, but not in conjunction with the core campaign. These spectra employed a 2688x512 Loral CCD with a resolution of $\approx$ 70,000 and covered the 6425–6445 Å region.

3. Ultraviolet Line Profiles

Initial spectral imaging studies of UV transitions (Walter et al. 1987, Neff et al. 1989) assumed that the intrinsic profiles could be modeled as gaussians. However, with the advent of GHRS, it became clear that simple gaussians are insufficient since very broad wings are detected in the TR profiles of several
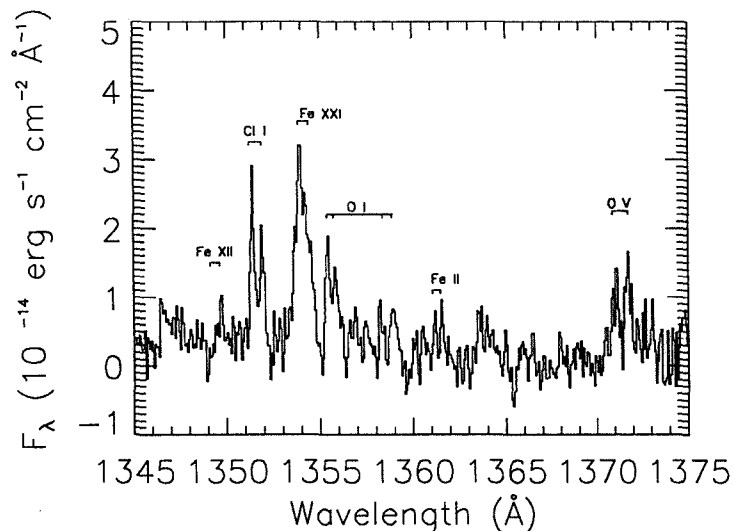
3

Figure 3. The Fe XXI region spectrum (ACCUM) of V824 Ara obtained near $\phi = 1906.4$ with key features identified. Results from this phase are discussed in greater detail in Airapetian & Dempsey (1997).

systems (Linsky & Wood 1994, Wood et al. 1995, Dempsey et al. 1996). Two component gaussian fits were used to fit the Mg II, C IV and Si IV profiles of V711 Tau (Wood et al. 1995, Dempsey et al. 1996). Although adequate fits to the observed line profiles may be obtained in this manner, the physical interpretation of the "broad" and "narrow" components is not clear. Wood et al. (1995) suggested that the broad component arises from microflares and Wood et al. (1997) derive a correlation between the width of this component in the C IV lines and the stellar X-ray flux. Dempsey et al. (1996) noted however, that, frequently, no unique decomposition could be obtained, making the derived widths somewhat arbitrary.

3.1. Two Gaussian Component Model

As in other late-type stars, the Mg II and C IV profiles for both stars in the V824 Ara system show very broad wings. Extended wings are also observed in at least the G-star component of He II. Initially, the profiles were modeled with 2 gaussians - one broad and one narrow. Fitting was performed using the Marquardt method (Bevington 1992) and included the GHRS PSF. However, it quickly became clear that the Mg II profiles differed in several key characteristics from those of the similar RS CVn binary, V711 Tau (HR 1099). A sample 2 component fit is shown in the top panel of Fig. 4. Free parameters in each component are the gaussian width, peak intensity and central position, for a total of 6 for each profile. In this fit, the gaussians parameters were allowed to vary in order to obtain the best fit. Note that, in this case, the broad component of the G-star completely swamps the narrow component, unlike models for the K-star component and other stars (see Wood et al. 1995, Dempsey et al. 1996). Furthermore, considerable variability is observed in the relative strengths of the 2 components at other phases; at several phases the intensity of the G-star narrow component is greater than that for the broad feature.

4

3.2. Anisotropic Macroturbulence Model

In order to try to improve on the model we applied the anisotropic turbulence (AT) model presented in Gray (1992). In this case, the line profile's shape results from the relative contribution of a radial macroturbulent velocity distribution $(\Theta_R(V_R))$ with fractional covering area A_R, and a tangential or horizontal distribution $(\Theta_T(V_T))$, covering area A_T. The distributions are assumed to be gaussian for a given $V_{R,T}$ while A_T is taken to be $1.0 - A_R$. The observed flux is then the standard convolution

$$F_\nu = \int I_\nu^o * (A_R\Theta_R(V_R) + A_T\Theta_T(V_T))cos\theta d\omega \tag{1}$$

integrated over the entire disk. The intrinsic line profile, I_ν^o, includes microturbulence (ξ), the rotational velocity (v $sini$), and linear limb brightening/darkening with coefficient ϵ. The PSF was included and again we used the Marquardt method of minimization. For each model, the central position (λ_{meas}), V_R, V_T, and peak intensity are free parameters for a total of 4 for each profile. Although ξ could be varied as well, little improvement is made in doing so. We used $\xi = 12$ km s^{-1}. In our models, $\epsilon = -0.2$. The results are shown in the lower panel of Fig. 4.

A comparison between the two models is given in Tables 1 & 2. Although the radial component dominates the profile, the tangential contribution is needed to fit the extended wings. Both fits have χ^2 around 0.10 and are very similar in quality, although the wings are fit slightly better in the AT model. Similar results are found for the Mg II k-line.

Finally, we applied the AT model to the $\phi = 2.73$ Mg II spectra of V711 Tau (see Dempsey et al. 1996) and list the results in Table 2 as well. Note that the velocities are significantly larger than we find for V824 Ara and the G star model profiles have no tangential contribution. This is consistent with the results of Robinson et al. (1996), who found that atmospheric turbulence was detected in all UV emission lines of V711 Tau and is anisotropically distributed purely along the radial or tangential direction (ignoring limb darkening).

These results suggest that anisotropic velocity distributions, perhaps generated by non-linear Alfvén waves, can produce the observed line profiles rather than heating by microflares. It is also the case that there are fundamental differences in the atmospheres of V824 Ara and V711 Tau. Analysis of the C IV, Si IV, O V, Fe XXI and He II profiles will allow us to map out the velocity structure throughout the atmosphere of V824 Ara and any changes as a function of phase.

References

Airapetian, V. & Dempsey, R. C. 1997, these proceedings

Bevington, P. R., 1992, Data Reduction and Error Analysis for the Physical Science (McGraw-Hill: New York)

Dempsey, R. C., Neff, J. E., Thorpe, M. J., Linsky, J. L., Brown, A., Cutispoto, G., & Rodonó, M. 1996, ApJ, 470, 1172
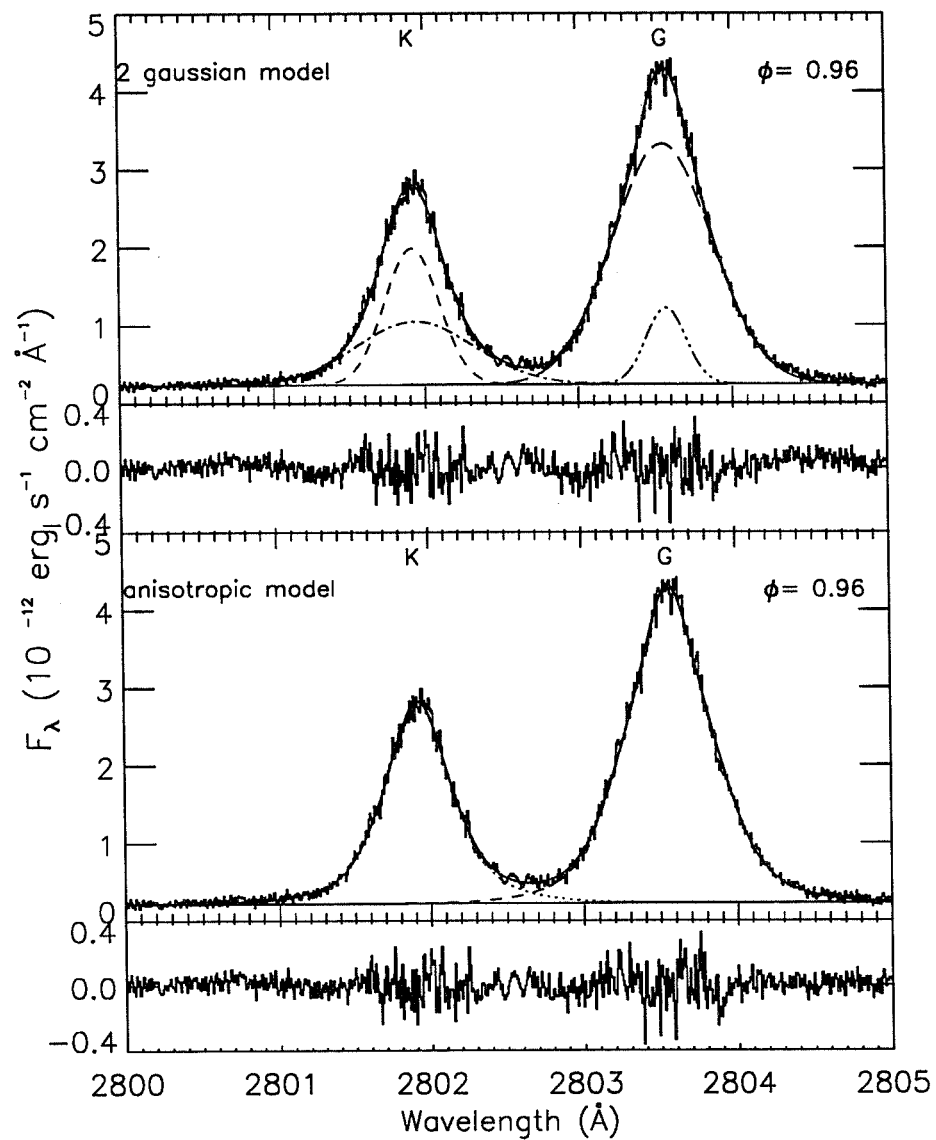
Figure 4.   The Mg II h profile at $\phi = 1906.96$ showing the best fit two gaussian component model and AT model. Residuals from the models are shown below each fit. For ease of fitting and visualization, the interstellar line has been approximately subtracted using 3 gaussians. For the AT model, *vsini* was taken to be 29 & 37 km s^{-1} for the K and G stars, respectively.

Donati, J.-F., Brown, S. F., Semel, M., Rees, D. E., Dempsey, R. C., Matthews, J. M., Henry, G. W. & Hall, D. S. 1992, 265, 682

Gray, D. 1992, in The Observation, & Analysis of Stellar Photospheres, (cambridge Univ. Press: New York), p407

Kürster, M, Schmitt, J, H. M. M. & Cutispoto, G. 1994, A&A, 289, 899

Linsky, J. L., & Wood, B. E. 1994, ApJ, 430, 342

Maran, S. P., et al. 1994, ApJ, 421, 800

Neff, J. E., Walter, F. M., Rodonò, M. & Linsky, J. L. 1989, A&A215, 79

Pasquini, L., Cutispoto, G. Gratton, R. & Mayor, M. 1991, A&A, 248, 72

Robinson, R., Airapetian, V., Maran, S. P., & Carpenter, K. G. 1996, ApJ, 469, 872

Rice, J. B. & Strassmeier, K. 1996, A&A, 316, 164

Richards, M. & Albright, G. 1996, in Stellar Surface Structure, ed. K. G. Strassmeier & J. L. Linsky, p 493

Strassmeier, K., G. 1996, A&A, 314, 558

Walter, F. M., Neff, J. E., Gibson, D. M., Linsky, J. L., Rodonó, M., Gary, D. E. & Butler, C. J. 1987, A&A186, 241

Wood, B. E., Harper, G. M., Linsky, J. L. & Dempsey, R. C. 1995, ApJ, 458, 761

Wood, B. E., Linsky, J. L. & Ayres, T. R. 1997, ApJ, 478, 745

Vogt et al., 1997, ApJS, submitted

Table 1.   2 gaussian model

Comp.	λ_{meas} Å	ΔV^a km s^{-1}	Width^b km s^{-1}	FWHM km s^{-1}	F_λ 10^{-12} erg s^{-1} cm^{-2}
K (narrow)	2801.916	-2.8	33.9 ± 3.3	78.0 ± 7.6	0.80 ± 0.03
K (broad)	2801.934	-4.8	73.0 ± 10.5	170.0 ± 24.4	0.80 ± 0.07
G (narrow)	2803.570	-8.1	24.4 ± 4.0	55.7 ± 9.1	0.32 ± 0.01
G (broad)	2803.552	-6.2	60.4 ± 2.0	140.7 ± 4.6	2.50 ± 0.03

^{a}Radial velocity with respect to predicted orbital position.
^{b}Gaussian width.

7

Table 2.   AT model

Comp.	λ_{meas} Å	ΔV^a km s^{-1}	V_R km s^{-1}	V_T km s^{-1}	A_R	F_λ 10^{-12} erg s^{-1} cm^{-2}
V824 Ara Mg II h-line $\phi = 1906.96$						
K0V-IV	2801.916	-2.9	33.6 ± 4.4	94.8 ± 11.8	0.80 ± 0.03	1.60
G5IV	2803.558	-6.7	45.0 ± 3.2	95.0 ± 9.5	0.85 ± 0.02	2.89
V824 Ara Mg II k-line $\phi = 1906.96$						
K0V-IV	2794.734	-0.5	44.1 ± 3.3	75.9 ± 10.4	0.88 ± 0.02	1.89
G5IV	2796.376	5.2^b	51.7 ± 2.2	129.3 ± 7.0	0.84 ± 0.01	3.79
V711 Tau Mg II h-line $\phi = 2.73^c$						
K1IV	2802.140	-4.6	100.2 ± 0.1	193.2 ± 0.5	0.98 ± 0.00	2.14
G5IV	2803.180	5.7	29.4 ± 0.1	...	1.00 ± 0.00	0.17
V711 Tau Mg II k-line $\phi = 2.73^c$						
K1IV	2794.970	-3.9	118.0 ± 0.1	181.0 ± 0.2	0.98 ± 0.00	2.91
G5IV	2795.920	-4.4	48.1 ± 0.1	...	1.00 ± 0.00	0.32

[a]Radial velocity with respect to predicted orbital position.

[b]Contaminated by the Mg II subordinate line at 2797.998 Å.

[c]Here $\xi = 15.9$ km s^{-1}, left as free parameter.

The RS CVn Binary HD 155555: A Comparative Study of The Atmospheres For The Two Component Stars

V. S. Airapetian

Computer Sciences Corporation, Astronomy Programs, NASA/GSFC, MD

R. C. Dempsey

Computer Sciences Corporation, STScI, Baltimore, MD

Abstract. We present GHRS/HST observations of the RS CVn binary system HD 155555 (see Dempsey et al., these proceedings). Several key UV emission lines (Fe XXI, Si IV, O V, C IV) have been analyzed to provide information about the heating rate throughout the atmosphere from the chromosphere to the corona. We show that both the G and K components reveal features of a chromosphere, transition region and corona. The emission measure distribution as a function of temperature for both components is derived and compared with the RS CVn system, HR 1099, and the Sun. The transition region and coronal lines of both stars show nonthermal broadenings of $\sim$ 20-30 km s^{-1}. Possible physical implications for coronal heating mechanisms are discussed.

1. Introduction

RS CVn binary systems represent a rich physical laboratory of magnetic activity where one or both (giant/subgiant G-/K-type star and late-type star/subgiant component) stars show strong soft X-ray, UV and radio emission and flare activity (Swank et al. 1981; Dempsey et al. 1993; Morris & Mutel 1988). ROSAT data suggested that coronae of these stars typically indicate a bimodal plasma temperature's distribution consisting of a warm 1-2 MK and a hot component with T = 10-20 MK. Recently GHRS/HST and EUVE observations of HR 1099 binary system show a strong emission at 1354Å from the Fe XXI ion formed at 10 MK and no significant emisson at 10^6K. Moreover, the HR 1099 system shows broad chromospheric, transition region and coronal lines while the K component reveals itself in Fe XXI 1354Å emission line without any observable flux in chromospheric lines (Robinson et al. 1996; Wood et al. 1996). Robinson et al. (1996) have discussed the nature of atmospheric heating in terms of non-linear surface Alfvén waves depositing its energy mostly in the transition region and contributing to the non-thermal broadening of UV lines formed at T= 0.1 - -0.3 MK.

HD 155555 is a short period (P=1.8 d) RS CVn binary system recently observed by the GHRS/HST and EUVE during the multiwavelength campaign (Dempsey et al. 1997). Pasquini et al. (1991) presented some evidence that

1

HD 155555 is a system composed of two young pre-main sequence stars. The objectives of the present study are to study two components separately in order to understand their evolutionary status (young main sequence component versus evolved subgiant) and atmospheric heating mechanisms. These unique, high-resolution data allow us to measure volumetric emission measures for both the G5 IV and K0V-IV components over a wide range of temperatures. Since the data were taken simultaneosuly we can compare the two spectral types directly. Furthermore, we can compare the results to those found for the RS CVn V711 Tau (HR 1099). In this paper we analyze the GHRS data obtained around phase 0.4. The data should not be affected in any way by the flare occuring near phase 0.6, however, phase related effects, although small, may be present. The EUVE data represent the flux integrated over the *entire* 5 day interval. Resolution in EUVE data are not adequate to resolve both stellar components.

2. GHRS, EUVE and ROSAT data: Comparative Analysis

2.1. Volumetric Emission Measures

GHRS/HST spectra near phase 0.4 clearly show the presence of emission from chromospheric, transition region and coronal lines belonging to the K- and G components and presents an unique opportunity for comparative study. In the Table 1 we present emission line fluxes from a number of lines forming throughout the stellar atmosphere with the temperature range from 10^4 to 10^7 K.

Table 1.   Emission Line Fluxes in 10^{-14} erg cm^{-2} s^{-1}

Emission Line	HR 1099	G/HD 155555	K/HD 155555
Chromosphere			
OI 1304 Å	130.0	4.34	3.0
SiII 1817.56 Å	135.0	9.8	6.6
Transition Region			
HeII 1640 Å	155.1	123.3	97.4
SiIV 1393 Å	75.5	9.32	4.95
CIV 1550 Å	313.2	18.0	13.7
OV 1371 Å	1.9	0.61	0.59
Corona			
FeXXI 1354 Å	3.1	1.9	8.89

It is evident that the flux ratio of the optically thin OV 1371Å line to the Fe XXI 1354Å for HR 1099 and the G component of HD 155555 is 0.6 and 0.3 respectively, while for the K component this ratio is only 0.07. We also see that the Fe XXI 1354 Åline flux from the K component of HD 155555 has the dominant contribution ($\sim$ 82 %) to the total emission from the binary system.

2

HD 155555 system has also been simultaneously observed by EUVE but the low spectral resolution does not allow us to resolve both components. Nevertheless, a comparative analysis of Fe XXI 1354Å emission in both components allows us to calculate the flux coming from the EUVE lines formed at T=10 MK from both components.

For an optically thin plasma the integrated flux, I_j, at the earth from a given emission line, j, can be estimated from the expression;

$$I_j = \frac{1}{4\pi d^2} \int_V P_j(N_e, T_e) \, N_e^2 \, dV \quad \text{erg cm}^{-2} \text{ s}^{-1} \text{ str}^{-1} \tag{1}$$

where P_j is the integrated line emissivity (in erg cm^3 sec^{-1}) and d is the distance to the star, N_e and T_e are the electron density in cm^{-3} and temperature respectively. For an isothermal plasma this can be written in terms of the volumetric emission measure, VEM $= \int_V N_e^2 \, dV$, as:

$$I_\lambda = \frac{1}{4 \pi d^2} P_\lambda(N_e, T_e) \, VEM, \tag{2}$$

From the observed line fluxes presented in Table 1 and EUVE line fluxes for UV lines from Fe XIII - Fe XXIII ions (Demspey et al. 1998) we calculate volumetric emission measures. Because emission from Fe XII 1349 Åhas not been detected we calculate the upper limit of the VEM from this line. In these calculations we have used line emissivity values tabulated by Monsignori-Fossi & Landini (1996) and Brickhouse et al. (1995). The results are presented in Table 2. In

Table 2.   VEM from GHRS and EUVE fluxes: K/HD 155555

Ion	Wavelength	VEM	Log T
CIV	1550Å	51.4	4.8
OV	1371Å	51.3	5.4
FeXII	1349Å	<51.7	6.0
FeXVIII	93.93Å	52.7	6.8
FeXIX	108.37Å	52.6	6.9
FeXX+XXI	118.66Å	52.6	7.0
FeXXI	117.51Å	53.3	7.0
FeXXI	1354Å	53.5	7.0
FeXXIII+XX	117.5Å	52.7	7.2

Fig. 1. we present a distribution of VEM over temperature adding the VEM values at 2 MK and 12.3 MK of the K component calculated by Dempsey et al. (1993) from the two-temperature thermal model. Here the triangles represent the VEM values from the GHRS/EUVE emission line fluxes and squares are the fluxes from ROSAT data. The VEM at T = 10 MK is scaled with the factor of 0.82. Fig. 1 shows that the VEM distribution of the K component
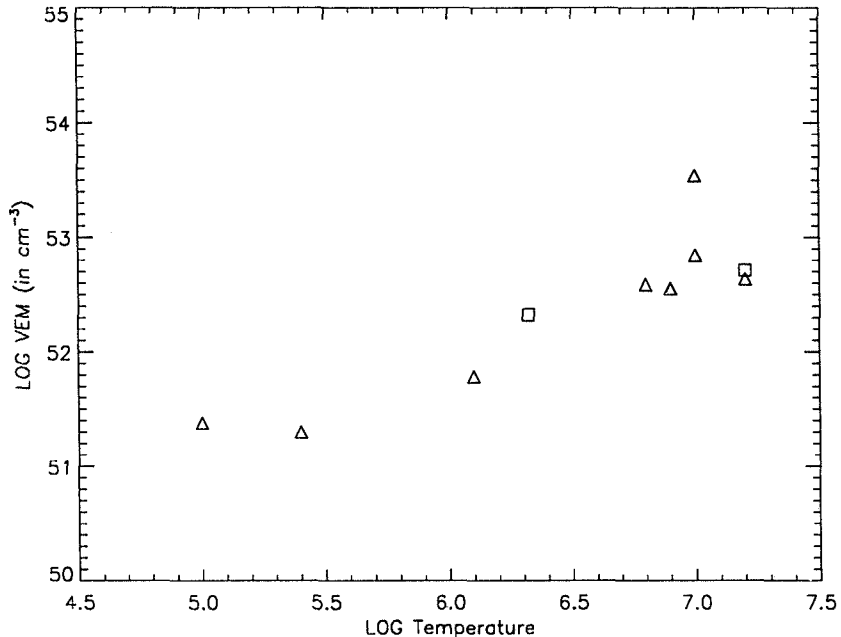
Figure 1. VEM distribution as a function of temperature for the K component of HD 155555

has a minimum at T =1 MK and a maximum at ∼ 10 MK which is typical for dMe stars, AT Mic and AU Mic (Monsignori Fossi et al. 1995, 1996). The VEMs derived from ROSAT data by Dempsey et al. (1993) are consistent with GHRS and EUVE data and, therefore, with the assumption of thermal nature of coronal plasma in the K therefore, with the assumption of the thermal nature of coronal plasma in therefore, with the assumption of thermal nature of coronal plasma in the K component. the K component.

Assuming for simplicity that the spherically symmetric corona is filled with semicircular magnetic loops (with a filling factor f) extending to radius R_*, all of which contains hot plasma, we have (Robinson et al. 1996)

$$VEM \sim N_e^2 V \sim f N_e^2 [\frac{4}{3}\pi(R^3 - R_*^3) - \pi R_*^2(R - R_*)] \qquad (3)$$

From the scaling law for the homogeneously heated quasistatic magnetic loop

$$N_e L = 9.12 \times 10^8 T_e^{\frac{19}{12}}, \qquad (4)$$

and equation 3 we find that the upper limit for loop length (if f=1) is $L_{loop} \approx 10^9$ cm and $N_e \approx 10^{11}$ cm^{-3}. Compact and high-density hot coronae were found also from EUVE data for dMe and RS CVn stars (Monsignori Fossi et al. 1996; Robinson et al. 1996).

The VEM distribution over temperature calculated for the G- component of HD 155555 and the active, K-component of HR 1099 is presented in Fig. 2.
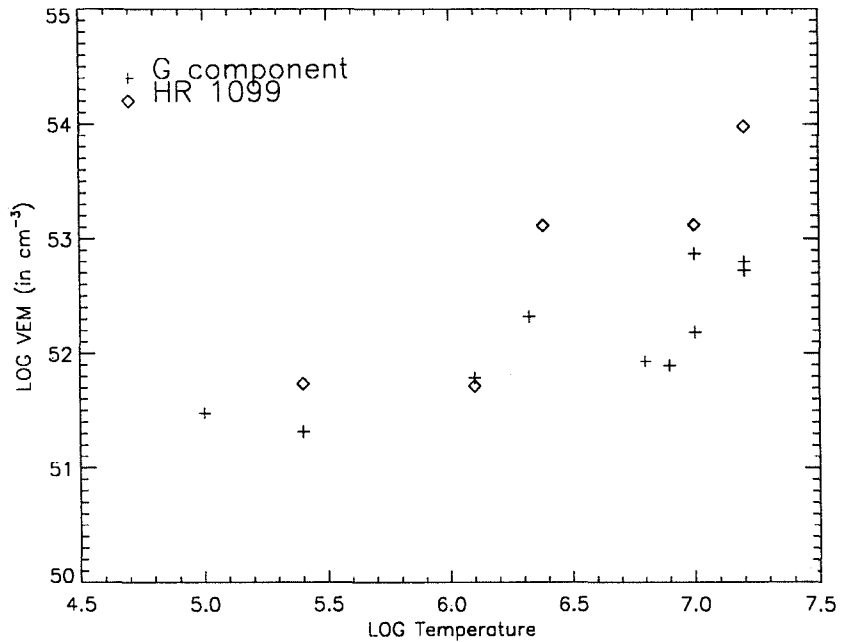
4

Figure 2.   VEM distribution for HR 1099 and G-components of HD 155555

We use GHRS, EUVE and ROSAT data for the G component of HD 155555 and GHRS and ROSAT data for HR 1099. VEM curves for both stars also show a minimum at T = 1 MK but do not show a pronounced maximum at 10 MK as for the K-component (see Fig 1) but have a monotonic growth of temperature for T > 1 MK. This is consistent with the VEM curves calculated for two other RS CVn systems, II Peg and λ And (Mitrou et al. 1996).

2.2.   Non-thermal Widths

Recent GHRS observations of the RS CVn system, HR 1099, have shown the presence of supersonic turbulent motions in the chromosphere and transition region of the G star with velocities up to 150 km s^{-1} as traced by nonthermal broadening of UV lines fromed throughout the atmosphere. Their line profiles can be accurately reproduced using a superposition of two Gaussian profiles and have been explained by the presence of anisotropic macroturbulence (Robinson et al. 1996). However, optically thin UV lines in AU Mic have profiles which can be fitted by a single Gaussian profile and have substantially smaller turbulent velocities than those observed in HR 1099. Our analysis of the UV lines of both two components of HD 155555 also shows that they reveal non-thermal or turbulent broadening. The results of line width calculations are presented in Table 3.

An asterisk denotes a presence of the two-Gaussian profile.

As we have shown above, HR 1099 and G component of HD 155555 also show similarity in the relatively large contribution of transition region fluxes in

5

Table 3. Turbulent velocities in HR 1099, G and K component of HD 155554

Emission Line	HR 1099	G	K	Log T
SiIV 1393Å	179.0*	42.7	34.7	4.8
HeII 1640Å	154.0*	159.0*	12.0	4.9
OV 1371Å	150.0*	≥ 39.3*	27.7	5.4
FeXXI 1354Å	65.0	35.3	20.0	7.0

OV 1371Å with respect to Fe XXI 1354Å and with the VEM distributions. These similarities can be understood in terms of one common mechanism of atmospheric heating. One possibility, heating due to dissipation of nonlinear surface Alfvén waves, has been described by Robinson et al. 1996.

Meantime, profiles of optically thin UV lines of the K component of HD 155555 are similar to the profiles of AU Mic and do not show strong nonthermal velocities or the presence of anisotropic turbulence. The ratio of OV (1371Å)/Fe XXI(1354Å) is much less than for the HR 1099 or G component. VEM distribution over temperature for the K component of HD 155555 is also similar to those observed in dMe star, AU Mic and in the solar atmsophere (Antonucci & Dodero 1995). These authors discussed such features in terms of heating due to microflares in the solar atmosphere.

3. Conclusion

Our comparative analysis of the K and G components of the RS CVn system, HD 155555, shows that

1. The G-component of HD 155555 shows a much larger ratio of OV 1371Å to Fe XXIÅ than the K component or either the active component in HR 1099.

2. The VEM distribution of the G-component of HD 155555 shows monotonic increase of the emission measure with temperature, while the VEM distribution for the K-component has a pronounced maximum at T=10 MK and is consistent with the curve characteristic of AT Mic and AU Mic.

3. The G-component of HD 155555 and the active component of HR1099 show features of significant anisotropically distributed macroturbulence, while the K-component of HD 155555 lacks these features similarly to the dMe stars, AT Mic and AU Mic and the Sun.

We suggest that the G-component of HD 155555 and the active component of HR 1099 have a common mechanism of atmospheric heating associated with dissipation of non-linear surface Alfvén waves in magnetic loops. However, the

K-component of HD15555, dMe stars and the Sun also show similar features of atmospheric heating and can be explained in terms of nano/microflares.

In conclusion, we note that the similarity of the K component of HD 155555 with dMe stars in a number of discussed features is consistent, in part, with the suggestion made by Pasquini et al. (1991) that HD 155555 is composed of two pre-main sequence star. At least, the K-component could be a young star with high-Li content. The G-component show features of a typical subgiant/giant RS CVn component.

References

Antonucci, E. & Dodero, M. A. 1995, ApJ, 438, 480 Brickhouse, N.S., Raymond, J.C., and Smith, B.W. 1995, A&AS, 97, 551

Dempsey, R. C. et al. 1997, this volume

Dempsey, R.C., Linsky, J. L., Schmitt, J. H. M. M. & Fleming, T. A. 1993, ApJ, 413, 333

Mitrou, C. K., Doyle, J. G., Mathioudakis & Antonopoulou 1996, Cool Stars 9, ASP Conf. Ser., 109, 275

Monsignori Fossi, B. C. & Landini, M. 1996,"The Arcetri Spectral code for Optically thin Plasmas", Astrophysics in the Extreme Ultraviolet, S.Bowyer and R.F. Malina (eds), 543

Monsignori Fossi, B. C., Landini, M., Drake, J. J., Cully, S. L. A&A, 302, 193

Monsignori Fossi, B. C., Landini, M., Del Aanna, G. & Bowyer, S. AJ, 466, 427

Morris, D. H. & Mutel, R. L. 1988, AJ, 95, 204

Pasquini, L., Gutispoto, G., Gratton, R. & Mayor, M. 1991, A&A, 248, 72

Robinson, R.D., Airapetian, V.S. Carpenter, K. & Maran S. 1996, ApJ, 469, 872

Swank, J. H., White, N. E., Holt, S. S. & Becker, R. H. 1981, ApJ, 246, 208

Wood, B.E., Harper, G.H., Linsky, J.L. & Dempsey, R.C. 1996, ApJ, 761

P/o 5-57788-2

S/3 - 89

????[1]

355640

ROBERT C. DEMPSEY

346988

Astronomy Programs, Computer Sciences Corporation,

Space Telescope Science Institute, 3700 San Martin Drive, Baltimore, MD 21218

P.55

Electronic mail: dempsey@stsci.edu

JAMES E. NEFF

KLAUS G. STRASSMEIER

University of Vienna, Institute for Astronomy,

Tuerkenschantzstr. 17, A-1180 Wien,

Austria

JEFFREY L. LINSKY

JILA, University of Colorado Boulder, CO 80309-0440

etc

ABSTRACT

TBD

Subject headings: stars: chromospheres – binaries: general – stars: late-type – stars: individual: V824 Ara – stars: rotation – stars: activity – stars: coronae

1. INTRODUCTION

TBD.

A number of studies, especially in recent years with the Hubble Space Telescope's (HST) Goddard High Resolution Spectrograph (GHRS), have been presented on the UV line profiles of late-type stars. generally, these consist of a few "snapshot" spectra of several different key diagnostic emission lines. From this it has become clear that many active stars possess non-gaussian line profiles. Unlike the case with AR Lac, observed with IUE (Walter et al. 1987; Neff et al. 1989), no *asymmetric* profile has been clearly identified that results from an inhomogeneous surface temperature or density distribution.

In 1993 we attempted to observe the RS CVn binary V711 Tau at several phases with the GHRS in a number of UV bandpasses in order to study profile variations as a function of phase (Dempsey et al. 1996). Unfortunately, scheduling problems, pointing errors, continuous flaring and the sparse and uneven phase sampling prevented us from achieving the primary goal. However, it is clear that a number of UV lines in the system, notably C IV, Si IV and Mg II show very extended emission out to several hundred km s^{-1}. The profiles were also clearly variable. Vilhu et al. (1997) and Walter et al. (1995) conducted a campaign on the rapidly rotating, single star AB Dor, where the observed C IV continuously for 14 hours. They found extended, non-gaussian emission in the C IV doublet and that Doppler images derived from these images were remarkably similar to the simultaneous spot-image. In a followup study of V711 Tau we have observed the another RS CVn with complete phase coverage in three key wavelength bandpasses, utilizing the ability of HST to observe some stars at high latitudes in uninterrupted fashion.

Generally classified as an RS CVn (see for example, Strassmeier et al. 1993), V824 Ara (HD 155555) consists of a G5 IV star in a short period orbit (P=1^d.68) with a K0 V-IV companion. However, the system does not eclipse and therefore does not rigorously fit

the Hall (1976) definition. There is also a visual M star companion (LDS587B) 33 arcsec away. The space velocities of the stars suggests that the binary is part of the young disk population which agrees with the high Li I $\lambda6708$ abundance (Pasquini et al. 1991). With the M star companion showing very high levels of activity it seems likely that the V824 Ara +LDS587B system is pre-main sequence. With rotational velocities of 37 km s^{-1} and 29 km s^{-1} for the G and K star components respectively, the system is very similar to V711 Tau. Photometric observations by Cutispoto (1993) show an amplitude, $\Delta V \approx 0.12$ with a period equal to the orbital value derived by Pasquini et al. (1991). Dempsey et al. (1993a) found a PSPC X-ray luminosity of 2.74 10^{30} erg s^{-1}. Two-temperature coronal models were applied to the PSPC X-ray pulse-height spectra by Dempsey et al. (1993b). They found that the lower temperature component was consistent with the full sample of RS CVn binaries studied but that the hot component was slightly lower than the sample as a whole. Moderate Ca II H and K emission, filled in IIα and radio emission (Strassmeier et al. 1993) are also consistent with this being a fairly active, short period binary system.

2. OBSERVATIONS

2.1. GHRS Observations

Observations with the GHRS were obtained when V824 Ara was in the CVZ of the HST. This means that the target is in view for approximately 9 HST orbits, each 96 minutes long, before the South Atlantic Anomaly (SAA) is crossed. During passage in the SAA the GHRS is paused due to the high radiation. For the next several orbits the SAA is crossed briefly followed again by 9 orbits of SAA free observing. Observations were scheduled to cycle between the C IV, Mg II and Fe XXI regions. In order to optimize observing efficiency this order was not always maintained if insufficient observing time was available to perform a full integration. Single observations at other wavelengths were obtained in order to

ascertain global atmospheric properties (e.g., emission measures) when small windows, too short for a full observation of one of the three key bandpasses, occurred in the schedule. In this manner observations of key chromospheric and TR regions lines such as Si IV, O IV, Si II, Si III], C III], O I, and He II were obtained. Since these lines were not the focus of this program no information about variability was obtained. An observing log is presented in Table ??. Due to a scheduling error at the STScI, the last 2 orbits of observing time were lost.

All observations were obtained with side 2 of the GHRS using the G160M grating, except for the Mg II data which used the Echelle-B grating. The Fe XXI spectra were readout out using the RAPID mode of the GHRS except for one observation (Z364030LT) so that good time resolution would be available in the event of a flare. In this mode the detector is readout in 1 second intervals. No quarter stepping is performed to reduce overhead so that there is virtually no dead time between readouts but detector granularity is retained in the data and spectral resolution is reduced slightly (1 diode $\approx$ 16 km s^{-1}). All other spectra, and Z364030LT, were obtained in FP-SPLIT ACCUM mode with quarter stepping. Spectral resolution is approximately 3.5 km s^{-1} diode^{-1} and 0.8 km s^{-1} diode^{-1} for the ECH-B and G160M data, respectively. Since orbital motion could be significant, thereby causing phase smearing of the line profiles, we observed with the large science aperture (LSA) to maximize throughput and keep exposure times as short as possible. To prevent the possible loss of significant amounts of data in the event of an instrument problem (e.g., grating carousel reset) the RAPID readout observations were broken up into paired exposures to prevent any large losses of data. Two wavelength calibration observations were shortened insignificantly by resets. One observation (Z364040QT) had a minor degradation of data caused by a brief loss of guide star fine lock. Affected readouts of this exposure were not used.

Wavelength calibration spectra were generally obtained prior to the start of each

observation in order to obtain the most accurate calibration possible. However, to ensure that the full integration time was obtained these could not always be scheduled. The GHRS SPYBAL positioning observation (Soderblom, Sherbert, & Hulbert 1993) was used if present and no other wavelength calibration was available. Previous studies have found that the default wavelength calibration is accurate to better than 1 km s^{-1} for the first-order gratings and 0.6 km s^{-1} for the Echelle-B grating. Using the calibration spectra taken at the time of the science observation improves the accuracy to approximately 0.1 km s^{-1}. Using the SPYBAL spectrum yields an accuracy somewhere in between the default calibration and that obtained with a contemporaneous comparison observation. An accuracy of better than 1 km s^{-1} is adequate for our analysis. All observations were calibrated in standard fashion using the GHRS Data Analysis Facility software current as of December 1993 (Blackwell et al. 1993). This calibration also includes correction for geomagnetic induced motion perturbation ("GIMP") which can induce velocity shifts over long exposures. Vignetting and flux calibration used the Robinson et al. (1993) values and are accurate to about 10%.

In Figures ?? and ?? we show all the Mg II and C IV ACCUM spectra as a function of phase. All orbital phases are computed using the Pasquini et al. (1991) ephemeris of HJD 2,446,998.4102 + 1.681652E. Phase 0.25 corresponds to conjunction with the K star in front. The remaining single-phase ACCUM spectra are displayed in Figure ??. The lone ACCUM spectrum of the Fe XXI wavelength region is shown in Figure ?? with several key features indicated.

During the entire observing campaign 48,313 spectra were obtained in RAPID readout mode at a sampling rate of 1 second. Observing in this mode is a tradeoff in that high time resolution is obtained at the expense of spectral resolution since quarter stepping of the grating is not performed. Maran et al. (1994) presented a detailed analysis of a large number of RAPID readouts of AU Mic which we followed with some small changes. Since binary orbital motion is significant in the V824 Ara system we cannot sum all the spectra

together. Furthermore, the count rate was lower than for AU Mic.

In addition to known turned-off diodes (Heap et al. 1995), it has recently become apparent that there are "flaky" diodes (Schultz & Bacinski 1996). These are diodes that are normal most of the time but occasionally do not register fully due to thermally induced, non-linear amplification effects in the detector Pre-Amp. Careful analysis of the diode behavior in conjunction with instrument temperature suggest that the effect may increase as the instrument warms up but no definitive correlation has yet been determined. Short observations tend not to experience this effect but these observations were obtained in the CVZ where solar heating of the aft shroud can be significant. Preparing for the second servicing mission, the GHRS observations were obtained with the FOS electronics also on in order to ascertain how the new instruments might affect the aft shroud temperature. In high S/N spectra it can be easy to identify their location and when they are not registering properly. However, with the low count rate observed for V824 Ara this is not possible.

In Fig. ?? we show the sum of all the rapid readout spectra. Several "hot" diodes, channels that always register the maximum value of 4096, can also be seen. The dead and intermittent diodes can easily be identified as negative spikes dropping below the "continuum", the latter having a value greater than zero. As a conservative strategy, since none of the intermittent diodes is near a key emission feature, we treated them in the same way we treated the dead diodes. For each readout, these diodes were set to the average value of adjacent diodes. Before final calibration and coaddition the data were "cleaned" of noisy readouts. Since the count rate in each 1 second scan is low, random noise or cosmic rays can introduce a significant amount of erroneous counts. Background counts can not be directly measured in RAPID readout mode unlike the case with ACCUM spectra. A delicate balance needs to be obtained in rejecting noisy readouts while not compromising real data. In Maran et al. (1994), the total counts in each readout were calculated, and, if that number exceeded a cutoff value it was rejected from the final spectrum. This cutoff

was determined from an estimate of the stellar flux, compared to the background level. The argument is that if the counts are above the cutoff it is probably noise and significant stellar signal is not lost if only a few readouts are removed.

We first examined all the counts for all the readouts (binned in a strong emission feature, a continuum region, and the whole 500 diode region) as a function of time and looked for short term variations or flares. Variations in the dark count as a function of HST's position in its orbit were readily apparent. No short term variations such as those reported by Soderblom et al. (1996), believed due to telescope "breathing" and calibration lamp voltage fluctuations, are evident and would not be expected since the LSA was used for the observations presented here. Except for the increase observed at several wavelengths around 1906.6, no obvious flares (e.g., count rates $\geq$ 3 standard deviations above the mean level) were detected but low level "microflaring" cannot be ruled out. Due to the low count rate even during the well defined flare (see below), short flares could not be distinguished from random noise. We could not use a high count rate in successive readouts as an indication of a flare since even during the strong flare around phase 1906.6, most elevated readouts were not adjacent to each other. To determine the "clean" cutoff value we looked at all the counts in a region thought to be relatively free of known emission lines and believed to represent continuum. In this way, we could determine the minimum, maximum and mean count rate per diode per readout expected. From this we concluded that a cutoff of 25 counts per readout was a reasonable choice. As a check, we adjusted the cutoff until the sum of the rejected readouts showed a statistically significant number of counts above the mean in the regions of the strong emission lines (i.e., Fe XXI and O V). Again, a cutoff of 25 yielded reasonably clean spectra. Although this method possesses some danger of removing real fluctuations when we know V824 Ara is variable, we feel that significant data have not been excluded since the rejected readouts are randomly scattered throughout each observation and amount to approximately 2% of the total exposure. Note that by definition

the resulting spectra may be "cleaned" of flare data as well. Count rates in rejected readouts were not sufficient to perform any analysis even if they could be clearly associated with a flare. The major rise in count rate during observation Z364060CT starts around readout 554 and continues until about scan 1161. This is only approximate since many readouts in between show zero counts since the count rate was still very low. Coadding all of these spectra was still insufficient in obtaining a flare spectrum with any useful S/N.

In Figure ?? we show the flux as a function of time during the Z364060CT exposure binned in 5 second intervals in 3 wavelength bands. The first light curve shows the flux in the entire 500 diode range as a function of time. A clear rise followed by a gradual decay is seen, possibly with a second, smaller flare around 1850 seconds after the start of the exposure. In attempt to determine if the flare occurred in the Fe XXI coronal feature, we also computed the total flux in a region centered on the Fe XXI and O I feature, the latter being included since it is heavily blended with the Fe XXI emission. Finally, we did the same for a region as free of obvious lines as possible, representing the continuum. As we show below this is not really a line free region but we obtained the same results for any other region we sampled. As is evident in Fig. ?? the flux increase is over the entire wavelength range and is not isolated to a few strong lines. Note that these data, in order to clearly see the time history, have not been cleaned in any way so that some of the smaller spikes are due most likely to noisy readouts.

An example of a coadded spectrum, its cleaned counterpart, and the sum of the rejected readouts is shown in Fig. ??. In Table ?? we list the spectra, the total number of readouts and the number of rejected readouts. Due to the resolution of the data in RAPID mode, the previously split RAPID exposures were coadded representing an integration time of nearly 75 minutes. These binned spectra are also indicated in Table ??. Since the extracted flare spectrum had too low of a S/N to be useful, and since the flare occurs over the entire wavelength region, we increased the cutoff to 40 during the 554-1161 readouts in

Z364060CT in order to retain the flare data. Some additional noise will be included. This is also consistent with the ACCUM data that were not "cleaned" of flare data since the flare dominants their entire exposure time.

Final calibration was performed in the same manner as for the ACCUM spectra except an extra calculation was required to correct for the dark count rate. The dark counts, as a function of geomagnetic latitude and longitude, were calculated from the Lindler et al. (1995) models and subtracted from the "cleaned" spectrum. Due to small count statistics, the integrated dark count rate was subtracted from the coadded, clean spectrum rather than from individual readouts before being summed. All spectra of the Fe XXI region as a function of phase are show in Figure ??. In some cases, the mean "continuum" level in the calibrated RAPID spectra is slightly below zero. We believe this results from the empirically derived Lindler et al. (1995) model overestimating the detector dark current.

2.2.   EUVE Observations

V824 Ara was observed by EUVE for 44 ksec simultaneously with the HST using the Short (SW), Medium (MW), Long (LW) wavelength, and DS detectors. Since V824 ara is not in the CVZ for the EUVE the observations contains gaps when the target was occulted by the earth. Due to a target of opportunity interrupting the observing program, this exposure time is less than half of what is required for reasonable S/N in the spectra. Due to the low count rate, insufficient counts were available to bin the spectra by time, even with a corse sampling. All spectra were reduced using the EUVE specific IRAF software and were processed using the optimal extraction routines in order to maximize S/N. In Figure ?? we show the SW spectra only since no emission features could be detected in the MW and LW bands. Here each channel equals 0.2 Å(900 km s^{-1}). At this resolution, and with a full cycle of orbital motion during the integration causing considerable phase

smearing, the two stellar components are not separable. In this spectrum the Fe XVIII (93.93Å) and Fe XXIII+Fe XX (132.8Å) are clearly visible while some weaker lines are marginally detectable. Counts due to the flare have not been removed from this spectrum due to the low overall count rate. It is also important to keep in mind that at least one flare was observed during the EUVE observation and and that the previously flat light curve exhibited considerable variability during the second have of the window (see below).

The DS photometer uses a Lexan boron filter with an effective bandpass of 40-190 Å, peaking around 90 Å. Good S/N is observable in the DS light curve which has been binned into XXX minute intervals as seen in Figure ??.

2.3. Radio Observations

2.4. Optical Spectroscopic Observations

2.5. Optical Photometric Observations

3. RESULTS

3.1. VARIABILITY

One of the prime goals of this project is to determine what, if any, variability is present in the V824 Ara system. Ideally, we would like to measure the line flux and profile shape as a function of phase for the UV lines.. Line profile shape and associated variations will be discussed in Section 3.2. In the case of V824 Ara, emission and absorption features of similar strength from both stellar components are observed in the spectra from the UV to the optical. This makes measuring the line properties near conjunction virtually impossible. For example, the 1345-1360 Å region spectra show the lines blended in almost half of the observed phases. Fitting the lines with gaussian profiles near conjunction requires fixing

many, or all, of the parameters to the values observed closer to quadrature, thereby making variability studies useless. The situation is better in the ACCUM spectra but line blends, e.g., the subordinate 2797.998 Å line of the Mg II k profile, are still prevalent.

To measure line fluxes we fitted the profiles with single, or in some cases, multiple gaussians. This will be further discussed in Section 3.2. These measurements can be found in Tables ??, ??, ?? and ??. Note that single gaussian were completely inappropriate for fitting the Mg II and C IV profiles. In Figure ?? we plot several key fluxes as a function of phase. In order to minimize the effect of blending we plot in the top panel the combined flux of Fe XXI and O I, although it appears that, within errors, the O I lines are virtually constant as is the case with the Cl I and O V features (not shown). The low point in the top panels comes from the ACCUM spectra and suggests a systematic difference between the data obtained with the two modes. It is apparent from the single ACCUM spectrum of this region that measurements of the lower resolution features include a significant contribution from the many, unresolved weak emission lines.

NOTE: have to have Mg II, C IV fluxes for light curve figures.

Most apparent from Figure ?? is the flare around 1906.60. It appears from the DS count rate that either two flares were observed or one with multiple phases. The first peak is clearly detected in C IV, possibly observed in the Mg II lines, but was missed due to an observing gap in the 1345–1360 Å region. The second DS peak corresponds to the flare observed in the 1345–1360 Å bandpass (see Fig. ??). Note that although the rise in flux in the Fe XXI+O I (Fig. ??) bandpass appears to be a marginal detection, the true measure of the flare is diluted in that the flare spectrum is combined with the non-flaring portion of Z364060CT and all of Z364060AT. No obvious rise in Mg II is detected at the second DS peak and unfortunately, there is no concurrent C IV observation. Since the photometry are not simultaneous to the other data, and would not likely show anything during the flare, we

can not conclude anything from these data other than the flare appears to have occurred as the major portion of the spot(s) rotated into view.

Outside of the flare only the photometry and possibly the C IV fluxes show any significant variability. This is not the case in subsequent days when both the DS count rate and the radio fluxes show considerable variability (see Section **XXX**). As discussed in Sections 3.2 and **??**, the flare appears to have occurred on or near the K-star, while the spots producing the visual matriculation wave are located on XXXX.

Reconcile different error bars used...

3.2. Line Profiles

3.2.1. Gaussian Models

In many situations, the UV line profiles can be fitted with a gaussian in order to measure line flux, profile width and doppler shift. With the advent of the GHRS, it has become clear that upper chromospheric and TR transitions such as Mg II, C IV and Si IV frequently show non gaussian structure in the form of very extended emission wings. Linsky & Wood (1994) discovered that the Si IV and C IV profiles of AU Mic (dMe) posses extended emission wings extending out ± 200 km s^{-1} from line center. Extended wings were also detected in the RS CVn V711 Tau (HR 1099; Wood et al. 1996, Dempsey et al. 1996) for Mg II and C IV. Similar wings were detected for Capella (Linsky et al. 1995) but not for the Mg II h and k lines. The lines of C IV in AB Dor, a young rapidly rotating K0-K2 IV-V single star, also have extended wings. Wood, & Linsky (1997) present a detailed analysis of C IV and Si IV line wings for a number of stars.

Since a single gaussian could not fit the line profiles, 2 gaussians were used. Generally, these line fits resulted in a "narrow" component and a "broad" component which dominates

the total line flux. The widths of the narrow feature, 10-50 km s^{-1}, imply that they are nonthermal in nature. In contrast, the width of the broad features is typically on the order of 100 km s^{-1} suggesting a thermal origin. Wood et al. (1996) have suggested that the broad gaussian component arises from TR "explosive events" similar to microflares and Wood & Linsky (1997) derive a correlation between the C IV broad component flux and the X-ray surface flux.

As a first step, we modeled all the GHRS profiles with single gaussians. Our approach is similar to that used in Dempsey et al. (1996). All fitting performed in this project is performed using the Marquardt method (Bevington 1992) as implemented in IDL. Each model includes a polynomial fit to the continuum and one or more gaussians, each with three free parameters: central wavelength, peak intensity and gaussian width. Generally, once the continuum was selected it was frozen and not allowed to vary. Results for these fits are shown in Fig. ?? and tabulated in Table ??. In the spectra of V824 Ara, the Mg II, C IV and the 1393 Å Si IV lines indicate extended wings for both stellar components. The G-star component of the He II 1640 Å profile also appears to possess extended wings. In the case of the Si IV profile, a simple broad-narrow model can fit the lines well with both components having the same relative velocity with respect to the predicted orbital positions. For He II, the best fit is obtained with a shifted broad component centered closest to the G star radial velocity. The line shift, and the shallowness of the gaussian, suggest that some contribution may be coming from extended wings of the K-star. However, at the single observed phase and S/N this cannot be ascertained. Results of these fits are listed in Table ?? and shown in Fig. ??. In both the single, and double gaussian fits, FWHM values are generally smaller than those observed for other well studied RS CVn systems such as V711 Tau (Dempsey et al. 1996; Wood et al. 1996), but are in the range of stars like β Cet (K0 III) and β Dra (G2 Ib-II; Wood & Linsky 1997).

In Wood et al. (1996) and Dempsey et al. (1996), the C III] profile for V711 Tau

appears broad and asymmetric. However, it was not clear from those data whether this was due to an unidentified blend or a transient feature. The only observation of the C III] line in V824 Ara indicates that it is considerably broader than if it were a single line. However, since the S/N is low, and the emission from both components are heavily blended ($RV_G = 12.8$ km s^{-1}, $RV_K = -8.0$ km s^{-1}) it is not possible to successfully model the profile with more than one gaussian. The Si III] profile at this same phase is slightly asymmetric, as one would expect for the relative line blending, but the width is still not comparable to that of C III]. If a transient had occurred we would expect it to show up in both profiles since their formation temperatures are similar, although not identical. Since only a single phase was observed its not possible to estimate the unblended contribution of each star to the line flux.

Two-component gaussian models for CI IV and Mg II for a single phase are given in Table ?? and shown in Figures ?? and ??. The narrow components have smaller FWHM values compared to V711 Tau, although the broad components are comparable in width. Note that in Fig. ?? the broad component of the G-star completely swamps the narrow component, unlike models for the K-star component and other stars (see Wood et al. 1995; Dempsey et al. 1996). Furthermore, considerable variability is observed in the relative strengths of the 2 components at other phases; at several phases the intensity of the G-star narrow component is greater than that for the broad feature.

How do the fits compare to W&L new relation?

Due to their low resolution, the EUVE emission lines and the RAPID readout GHRS line profiles were only fit with single gaussians. These results are listed in Tables ?? and ??.

3.2.2. Anisotropic Models

Although reasonable fits to the C IV and Mg II may be obtained with multiple gaussians, close inspection shows that the extended emission wings are still not perfectly matched. Vilhu et al. (1997) modeled the C IV profiles of AB Dor with a constant broad component combined with a variable narrow gaussian from which they derived a chromospheric Doppler image. In the case of V824 Ara the wings are highly variable and could not be modeled with a constant gaussian. In order to see if we could improve the fit and perhaps obtain a model with a clearer theoretical interpretation we applied the anisotropic turbulence (AT) model presented in Gray (1992). This model was also successfully applied to the O V profile in V711 Tau by Robinson et al. (1996). In the AT model, the line profile's non-gaussian shape results from the relative contribution of a radial macroturbulent velocity distribution ($\Theta_R(V_R)$) with fractional covering area A_R, and a tangential or horizontal distribution ($\Theta_T(V_T)$), covering area A_T. The distributions are assumed to be gaussian for a given $V_{R,T}$ while A_T is taken to be $1.0 - A_R$ for simplicity. The observed flux is then the standard convolution

$$F_\nu = \int I_\nu^o * (A_R\Theta_R(V_R) + A_T\Theta_T(V_T))cos\theta d\omega \tag{1}$$

integrated over the entire disk where θ is the angle between the line of sight and the turbulent motion. The intrinsic line profile, I_ν^o, includes microturbulence (ξ), the rotational velocity ($v\sin i$), and linear limb brightening/darkening with coefficient ϵ. The PSF (REF) was included and again we used the Marquardt method of minimization. For each model, the central position (λ_{meas}), V_R, V_T, and peak intensity are free parameters for a total of 4 for each profile. Although ξ could be varied as well, little improvement is made in doing so. The results were weakly dependent upon ξ and ϵ so we chose to fix these parameters in order to somewhat constrain the models. In our models, we used $\epsilon = -0.2$ and $\xi = 12$ km s^{-1}. The results are shown in the lower panel of Fig. ??.

A comparison between the two models is given in Tables ?? & ??. Although the radial component dominates the profile, the tangential contribution is needed to fit the extended wings. Both fits have χ^2 around 0.10 and are very similar in quality, although the wings are fit slightly better in the AT model. Similar results are found for the Mg II k-line.

In either scheme - 2 gaussian or AT - modeling two stellar profiles as a function of phase is extremely challenging. In the case of AB Dor, the C IV modeling of Vilhu et al. (1997) was for a single star where rotation dominates all other line broadening processes. Due to their lower visibility, to properly characterize the extended wings requires that as much of their extent as possible is visible. Near conjunction up to half of the line wing may be "lost" in the profile of the companion star while at conjunction the wings represent a combination of both flux from both stars. Since both profiles are clearly variable, with fluctuations in the line core as well as the wings, we decided to not model the profiles as a function of phase but rather will look at the variability in general. In a later paper we will perform true Doppler imaging. Therefore, we obtained the best model to the first observation of Mg II and C IV. Since these data were taken near quadrature the individual line profiles are well seperated and the least blended. We then subtracted the model profiles from ?? as a function of phase, shifting the profiles into the rest frame of the stars at each epoch.

For example, we show the results for the Mg II h-line in Fig. ??. Here the AT model from Table ?? was subtracted from all the other phases. A gaussian was used fit to the IS line at this phase. At subsequent phases, a gaussian with the same FWHM (0.06Å), wavelength (2802.530Å) and equivalent width (0.33Å) was used. Since the IS line is saturated at ϕ =1905.96 since it overlies the weak K-star emission, this gaussian fit under estimatets the IS contribution at later phases. Since we are interested in the changes from the system at the first phase this is acceptable. Alternatively, we could use a fit to the ϕ =1906.46 or 1906.53 observation but since this is close to the flare we chose not to use

these data for this purpose. The vertical lines in Fig. ?? shows the region affected by the IS line. Clearly, a great deal of the deviation from zero around this region is due to improper correction of the IS contribution. However, significant changes can be seen rather far from this region, especially around the flare, and then again near phase 1906.88. the IS line at this phase and subtracted.

Well, I don't know how good this is and if worth doing to the k and CIV. CIV might be better since no IS line.

3.3. Flares

3.4. Doppler Imaging

4. DISCUSSION

- Note that the AT model 2 velocity components may be the same sort of thing Vilhu et al. (1997) saw for AB Dor but attributed to prominences; and may be another way to parameterize the Wood-Linsky microflare broad comp.

Table 1: Summary of Observations

Observation ID	Region	HJD (+2450000)	P_{orb}	t_{exp} sec
Z3640109T	C IV	203.5505	1905.9474	1523.2
Z364010CT	Mg II	203.5703	1905.9592	761.6
Z364010GT	Fe XXI	203.5974	1905.9753	2259.2
Z364010IT	Fe XXI	203.6260	1905.9923	2232.2
Z364010LT	C IV	203.6550	1906.0096	1523.2
Z364010OT	Mg II	203.6754	1906.0217	761.6
Z364010ST	Fe XXI	203.7017	1906.0373	2250.2
Z364010UT	Fe XXI	203.7300	1906.0542	2263.2
Z364010WT	He II	203.7552	1906.0692	1523.2
Z3640207T	C IV	203.8102	1906.1018	1523.2
Z364020AT	Mg II	203.8300	1906.1136	761.6
Z364020ET	Fe XXI	203.8560	1906.1291	2264.2
Z364020GT	Fe XXI	203.8845	1906.1460	2249.2
Z364020JT	C IV	203.9131	1906.1630	1523.2
Z364020MT	Fe XXI	203.9412	1906.1798	2263.2
Z364020OT	Fe XXI	203.9697	1906.1967	2256.2
Z364020RT	Mg II	203.9995	1906.2144	761.6
Z364020TT	Si III],C III]	204.0200	1906.2266	‑1196.8

(continued)

Table 1: Summary of Observations

Observation ID	Region	HJD (+2450000)	P_{orb}	t_{exp} sec
Z3640306T	Mg II	204.0558	1906.2479	544.0
Z364030AT	Fe XXI	204.0929	1906.2700	2054.2
Z364030CT	Fe XXI	204.1190	1906.2855	2053.2
Z364030FT	C IV	204.1666	1906.3138	1849.6
Z364030IT	Mg II	204.1887	1906.3269	1088.0
Z364030LT	Fe XXI[a]	204.2299	1906.3514	3699.2
Z364030NM	C IV	204.2803	1906.3814	1414.4
Z364030QT	Mg II	204.3062	1906.3968	761.6
Z364030ST	Si IV,O IV	204.3156	1906.4024	435.2
Z3640407T	C IV	204.3814	1906.4415	1523.2
Z364040AT	Mg II	204.4012	1906.4533	761.6
Z364040ET	Fe XXI	204.4428	1906.4781	2265.2
Z364040GT	Fe XXI	204.4713	1906.4950	2264.2
Z364040JT	C IV	204.5000	1906.5121	1523.2
Z364040MT	Mg II	204.5197	1906.5238	761.6
Z364040QT	Fe XXI	204.5459	1906.5394	2201.2
Z364040ST	Fe XXI	204.5743	1906.5563	2248.2
Z364040UT	O I	204.5996	1906.5713	1523.2
Z3640507T	C IV	204.6500	1906.6013	1523.2

(continued)

Table 1: Summary of Observations

Observation ID	Region	HJD (+2450000)	P_{orb}	t_{exp} sec
Z364050AT	Mg II	204.6699	1906.6131	761.6
Z364050ET	Fe XXI	204.6959	1906.6285	2256.2
Z364050GT	Fe XXI	204.7247	1906.6456	2205.2
Z364050JT	C IV	204.7530	1906.6625	1523.2
Z364050MT	Mg II	204.7729	1906.6743	761.6
Z364050QT	Fe XXI	204.7998	1906.6903	2248.2
Z364050ST	Fe XXI	204.8282	1906.7072	2247.2
Z364050VT	Mg II	204.8525	1906.7216	761.6
Z3640606T	Mg II	204.8867	1906.7420	544.0
Z364060AT	Fe XXI	204.9099	1906.7558	2053.2
Z364060CT	Fe XXI	204.9361	1906.7714	2034.2
Z364060FT	C IV	204.9653	1906.7888	1849.6
Z364060IT	Mg II	204.9890	1906.8028	1088.0
Z364060MT	Fe XXI	205.0314	1906.8281	2048.2
Z364060OT	Fe XXI	205.0458	1906.8367	2035.2
Z364060RT	C IV	205.0993	1906.8684	1414.4
Z364060UT	Mg II	205.1185	1906.8798	761.6
Z364060WT	Si II	205.1299	1906.8866	544.0

[a]ACCUM mode, all other Fe XXI spectra are RAPID.

Table 2: Rapid Readout Observation Processing Log

Observation	n^a	$n_r{}^b$	c^c cnts	Observation	n	n_r	c cnts	ϕ^d
Z364010GT	2258	32	25.88	Z364010IT	2231	41	24.64	1905.98
Z364010ST	2249	52	28.83	Z364010UT	2262	50	27.73	1906.04
Z364020ET	2263	50	26.35	Z364020GT	2248	53	29.97	1906.14
Z364020MT	2262	95	28.23	Z364020OT	2255	44	24.36	1906.19
Z364030AT	2053	36	20.80	Z364030CT	2052	46	21.62	1906.28
Z364040ET	2264	68	22.38	Z364040GT	2263	33	23.61	1906.49
Z364040QT	2200	42	26.08	Z364040ST	2247	37	25.68	1906.55
Z364050ET	2255	50	25.89	Z364050GT	2204	47	25.74	1906.64
Z364050QT	2247	59	25.55	Z364050ST	2246	58	26.15	1906.70
Z364060AT	2052	89	24.75	Z364060CT	2033	89^e	18.02	1906.76
Z364060MT	2047	37	20.59	Z364060OT	2034	116	21.40	1906.82

[a]Number of readouts.

[b]Number of rejected readouts.

[c]Integrated dark count rate.

[d]Mean phase of combined observations.

[e]During the readouts between 554-1161 the cutoff was raised to 40.

Table 3.   1345–1360ÅLine Measures

| Phase | F_λ | | FWHM | | ΔV^a | |
| | 10^{-14} erg s^{-1} cm^{-2} | | km s^{-1} | | km s^{-1} | |
	G	K	G	K	G	K
Cl I 1351.657 Å						
1905.98	1.67±0.01	1.00±0.01	55±1	50±1	3±1	14±1
1906.04	1.67±0.04	1.09±0.04	55±1	56±2	3±1	9±1
1906.14	1.89±0.01	1.26±0.01	61±1	54±1	13±1	22±1
1906.19	2.66±0.01		99±1		⋯	⋯
1906.28	2.52±0.01		83±1		⋯	⋯
1906.35	0.87±0.03	0.62±0.03	73±10	67±16	0±4	-6±6
1906.49	1.47±0.01	0.86±0.01	64±1	47±1	6±1	4±1
1906.55	1.81±0.25	0.93±0.25	62±3	49±5	1±1	-2±2
1906.64	1.37±0.01	1.20±0.01	58±1	51±1	15±1	7±1
1906.70	3.08±0.01		83±1		⋯	⋯
1906.76	3.12±0.14		62±1		⋯	⋯
1906.82	1.66±0.01	1.15±0.01	55±1	38±1	-1±1	52±1
Fe XXI 1354.14 Å						
1905.98	3.33±0.01	2.51±0.01	119±1	211±4	8±1	14±2
1906.04	1.71±0.31	3.63±0.36	99±5	229±12	23±2	78±8
1906.14	2.48±0.63	2.30±0.49	134±4	154±6	23±4	35±7
1906.19	5.31±0.01		149±1		⋯	⋯
1906.28	5.63±0.01		139±1		⋯	⋯
1906.35	1.86±0.03	1.03±0.03	150±10	145±36	-3±9	2±17
1906.49	3.97±0.01	1.02±0.01	164±1	84±1	2±1	4±1
1906.55	2.89±3.10	2.60±3.68	157±19	194±40	-17±15	-39±28
1906.64	3.72±0.01	1.75±0.01	125±1	91±2	4±1	20±1
1906.70	6.82±0.01		146±1		⋯	⋯
1906.76	5.37±0.14		138±3		⋯	⋯
1906.82	1.06±0.03	4.13±0.04	63±2	134±2	-39±1	56±1
O I 1355.598 Å						
1905.98	1.53±0.01	1.13±0.01	78±1	76±1	21±1	18±1
1906.04	1.22±0.04	0.81±0.04	78±3	68±3	22±1	19±1
1906.14	2.29±0.01	0.40±0.01	111±1	37±1	21±1	19±1
1906.19	2.49±0.01		102±1		⋯	⋯

Table 3—Continued

Phase	F_λ 10^{-14} erg s^{-1} cm^{-2}		FWHM km s^{-1}		ΔV[a] km s^{-1}	
	G	K	G	K	G	K
1906.35	0.43±0.05	0.76±0.07	52±16	124±46	15±6	-6±18
1906.49	1.28±0.01	0.88±0.01	79±1	92±1	22±1	20±1
1906.55	1.41±0.28	1.29±0.26	58±4	97±9	20±2	8±4
1906.64	0.83±0.01	1.66±0.01	64±2	91±2	19±1	12±1
1906.70	2.95±0.01		98±1		⋯	⋯
1906.76	2.89±0.14		82±2		⋯	⋯
1906.82	1.10±0.02	1.28±0.02	77±3	90±3	-34±1	70±1

O V 1371.292 Å

Phase	F_λ		FWHM		ΔV[a]	
1905.98	1.17±0.01	0.50±0.01	101±1	71±1	22±1	28±1
1906.04	0.47±0.01	0.32±1.46	54±3	77±2	7±1	36±2
1906.14	0.88±0.12	0.80±0.15	67±6	92±12	34±2	24±5
1906.19	1.70±0.01		130±2		⋯	⋯
1906.28	0.27±0.01		30±2		⋯	⋯
1906.35	0.65±0.05	0.63±0.05	117±5	92±5	-10±1	32±1
1906.49	0.78±0.01	0.72±0.01	88±1	76±1	29±1	21±1
1906.55	0.96±0.35	0.85±0.41	96±16	112±24	24±6	15±10
1906.64	0.49±0.01	1.00±0.01	56±2	89±1	34±1	19±1
1906.70	0.53±0.01		67±1		⋯	⋯
1906.76	1.73±0.19		109±8		⋯	⋯
1906.82	0.89±0.01	1.12±0.01	78±1	127±2	-27±1	71±3

[a]Radial velocity with respect to predicted orbital position.

Table 4. One Component Gaussian Fits

Phase	F_λ		FWHM		ΔV^a	
	10^{-14} erg s^{-1} cm^{-2}		km s^{-1}		km s^{-1}	
	G	K	G	K	G	K
O I 1304.858 Å						
1906.57	5.12±0.01	4.63±0.01	77±1	53±1	8±1	-9±1
O I 1306.029 Å						
1906.57	3.05±0.01	4.42±0.01	56±1	56±1	2±1	-11±1
Si IV 1393.755 Å						
1906.40	10.39±0.34	4.89±0.32	110±6	90±8	1±2	1±3
Si IV 1402.770 Å						
1906.40	3.99±0.52	2.63±0.88	83±11	112±37	-3±5	-20±16
He II 1640.428 Å						
1906.07	28.72±0.08	19.37±0.08	83±1	71±1	15±1	19±1
Si II 1808.012 Å						
1906.89	5.71±0.07	7.84±0.07	69±2	73±2	-7±1	-3±1
Si II 1816.928 Å						
1906.89	6.63±0.01	9.63±0.03	49±1	58±1	-18±1	-9±1
Si II 1817.451 Å						
1906.89	1.73±5.29	4.18±0.02	46±46	53±1	-29±1	-8±1
Si III] 1892.030 Å						
1906.23	4.69±0.54		92±13		⋯	⋯
S I 1900.268 Å						
1906.23	1.44±0.55		45±14		⋯	⋯
C III] 1908.734 Å						
1906.23	1.63±0.54		204±120		⋯	⋯
S I 1914.698 Å						
1906.23	1.53±0.52		154±79		⋯	⋯

Table 5.   Two Component Gaussian Fits

| Phase | F_λ | | FWHM | | ΔV[a] | |
| | 10^{-14} erg s^{-1} cm^{-2} | | km s^{-1} | | km s^{-1} | |
	G	K	G	K	G	K
He II 1640.428 Å						
1906.07[b]	24.68±0.20	17.21±0.15	76±1	67±1	15±1	19±1
1906.07[c]	9.18±0.59	⋯	359±24	⋯	7±12	⋯
Si IV 1393.755 Å						
1906.40[b]	4.41±0.81	1.68±0.43	67±9	48±11	1±2	3±3
1906.40[c]	7.14±0.50	3.70±0.40	224±36	226±57	1±2	4±3
C IV 1548.202 Å						
1905.95[b]	8.77±0.18	8.69±0.08	62.2±5.0	65.6±4.3	18.1±1.0	15.2±1.0
1905.95[c]	20.09±0.48	10.78±0.17	170.1±12.2	223.3±23.2	18.1±1.0	15.2±1.0
C IV 1450.774 Å						
1905.95[b]	7.00±0.12	4.43±0.08	73.4±7.3	57.7±7.0	21.1±1.5	18.6±1.7
1905.95[c]	9.71±0.30	5.20±0.22	204.8±43.8	209.6±26.0	21.1±1.5	18.6±1.7
Mg II 22795.530 Å						
19065.96[b]	78.4±2.2	58.8±5.5	46.1±3.7	43.3±6.1	5.1±0.8	0.7±1.1
19065.96[c]	282.2±4.9	135.7±10.7	94.7±3.3	81.2±6.4	4.1±0.7	1.8±1.3
19065.96[d]	7.0±0.1	7.9±0.1	41.8±13.1	52.6±15.0	4.6±5.6	≡ 0
Mg II 2802.695 Å						
19065.96[b]	0.32±0.01	0.80±0.03	55.7±9.1	78.0±7.6	-8.1±1.0	-2.8±2.0
19065.96[c]	2.50±0.03	0.80±0.07	140.7±4.6	170.0±24.4	-6.2±0.7	-4.8±1.7

[a]Radial velocity with respect to predicted orbital position.

[b]Narrow component.

[c]Broad component.

[d]Subordinate Mg II k-line at 2797.998 Å.

Table 6.   EUVE Line Measures

ID	F_λ
	10^{-14} erg s^{-1} cm^{-2}
Fe XVIII	9.98±0.03
Ne VIII	12.32±0.01
Fe XXI	11.17±0.01
Fe XIX	9.74±0.01
Fe XXII+Fe XXI	9.28±0.01
Fe XX	7.28±0.01
Fe XXIII+Fe XX	29.44±0.01

REFERENCES

Bevington, P. R., & Robinson, D. K. 1992, Data Reduction and Error Analysis for the Physical Science (McGraw-Hill: New York), p. 161

Blackwell, J., Shore, S. N., Robinson, R. D., Feggans, K., Lindler, D., Malumuth, E., Sandoval, J. & Ake, T. B. 1993, in *A User's Guide to the GHRS Software Version 2.1*, GHRS internal document

Dempsey, R. C., Neff, J. E., Thorpe, M. J., Linsky, J. L., Brown, A., Cutispoto, G., & Rodonó, M. 1996, ApJ, 470, 1172

Dempsey, R. C, Linsky, J. L., Schmitt, J. H. M. M. & Fleming, T. A. 1993a, ApJS, 86, 599

Dempsey, R. C, Linsky, J. L., Schmitt, J. H. M. M. & Fleming, T. A. 1993b, ApJ, 413, 333

Donati, J.-F., Brown, S. F., Semel, M., Rees, D. E., Dempsey, R. C., Matthews, J. M., Henry, G. W. & Hall, D. S. 1992, 265, 682

Gray, D. 1992, in The Observation, & Analysis of Stellar Photospheres, (cambridge Univ. Press: New York), p407

Heap, S. R. et al. 1995, PASP, 107, 871

Kürster, M, Schmitt, J, H. M. M. & Cutispoto, G. 1994, A&A, 289, 899

Lindler et al. (1995)

Linsky, J. L., & Wood, B. E. 1994, ApJ, 430, 342

Linsky, J. L., Wood, B. E., Judge, P., Brown, A., Andrulis, A. & Ayres, T. 1995, ApJ, 442, 360

Maran, S. P., et al. 1994, ApJ, 421, 800

Neff, J. E., Walter, F. M., Rodonò, M. & Linsky, J. L. 1989, A&A215, 79

Pasquini, L., Cutispoto, G. Gratton, R. & Mayor, M. 1991, A&A, 248, 72

Robinson, R. 1993

Robinson, R., Airapetian, V., Maran, S. P., & Carpenter, K. G. 1996, ApJ, 469, 872

Schultz, A.B. & Baciniski, J. 1996, GHRS Instrument Science Report No. 78

Soderblom, D. S., Sherbert, L. E. & Hulbert, S. J, 1993, in *Calibrating the Hubble Telescope*, ed J. Chris Blades and Samantha J. Osmer, Space Telescope Science Institute, p. 264

Soderblom, D. S., Eisenhamer, J., Hulbert, S., Leitherer, McGrath, M., Sherbert, L. & Skapik, J. 1996, GHRS Instrument Science Report No. 73

Strassmeier, K. G., Hall, D. S., Fekel, F. C. & Scheck, M. 1993, A&AS, 100, 173

Walter, F. M., Neff, J. E., Gibson, D. M., Linsky, J. L., Rodonó, M., Gary, D. E. & Butler, C. J. 1987, A&A, 186, 241

Walter, F. M., Collier-Cameron, A., Suntzeff, N., Kürster, M., Vilhu, O., Slee, B., 1995, BAAS, 187

Wood, B. E., Harper, G. M., Linsky, J. L. & Dempsey, R. C. 1996, ApJ, 458, 761

Wood, B. E., Linsky, J. L. & Ayres, T. R. 1997, ApJ, 478, 745

Wood, B. E. & Linsky, J. L. 1997, ApJ, submitted

Vilhu, O., Muhli, P., Huovelin, J., Hakala, P., Rucinski, S. M., Collier Cameron, A. 1997, AJ, submitted

F$_\lambda$ (10^{-12} erg s^{-1} cm^{-2} Å^{-1})

Wavelength (Å)
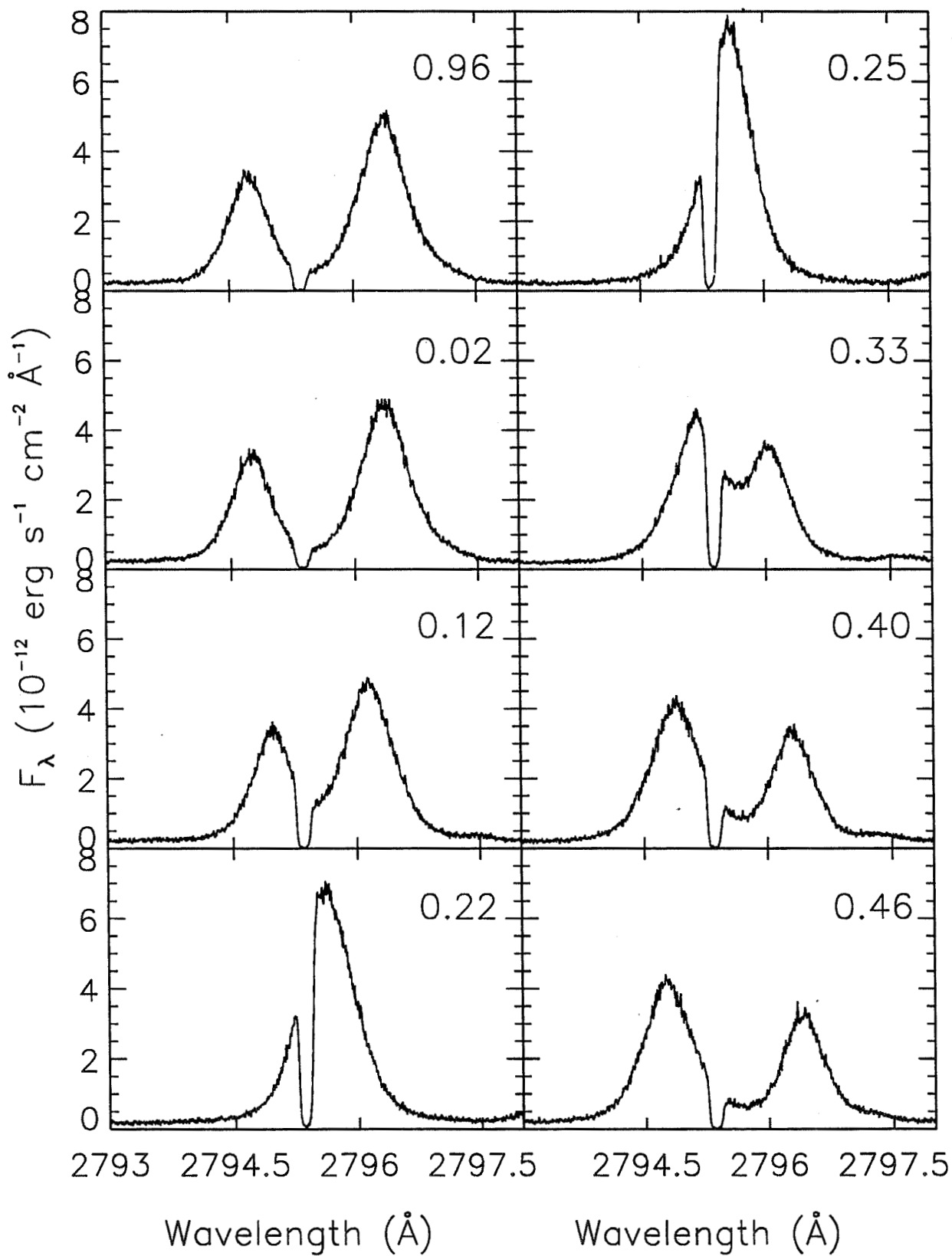
Fig. 2.— All C IV spectra as a function of phase.

Fig. 3.— Miscellaneous single-phase spectrum with key features indicated. Note that due to low S/N all spectra above, except the He II region, have been binned at a ratio of 4 bins to 1.

Fig. 4.— ACCUM spectrum of the Fe XXI region spectrum showing several key features.

Fig. 5.— All rapids summed into a single spectrum showing the dead and intermittent diodes.

Fig. 6.— Example of RAPID readout cleaning using Z364010IT. The top panel is the coaddition of 2231 readouts where bad or intermittent diodes have been reset. The middle panel is the same spectrum minus the 41 rejected readouts and with the removal of the integrated dark current rate, in this case equal to 24.64 counts. In the bottom panel we show the sum of the 41 rejected spectra. Note that this example shows the worst case situation where the algorithm used may have rejected a few counts of the Cl I lines but this represents only a few percent of the total.

Fig. 7.— Time history of flare as observed in the Fe XXI region GHRS spectra. The top panel shows the integrated flux over the entire 500 diode range as a function of time with zero corresponding to the start of the Z364060CT exposure. In the second and third panels we show the integrated flux in two 46 diode wavelength regions, the first centered on the FeXXI+OI features and the second covering a line free or "continuum" region ($\approx$ 1345-1347Å). A bin size of 5 seconds is used for all panels and the dark count rate has been removed. These data have not been "cleaned" of noisy readouts and include the entire observation.

Fig. 8.— Final reduced spectra of the Fe XXI region as a function of phase. The ACCUM spectra is shown at phase 1906.37.

Fig. 9.— EUVE SW spectrum with several key lines indicated.

Fig. 10.— The entire EUVE DS light curve as a function of observing phase.

Fig. 11.— Multiwavelength light curves for V824 Ara as a function of phase. Note that the shown photometry is not simultaneous with the other observations but are, instead, a folded set of data as described in the text. Error bars for the GHRS data are estimated from repeated measurements of several lines in each bandpass, purposely choosing overly high and low continuum levels. In this fashion, we conservatively estimate errors of 10%, 5% and 2% for the Fe XXI + O I, Mg II (h+k), and C IV line fluxes, respectively. Placement of the continuum is the largest source of error in these measurements. Note that the fluxes, F_λ, are in units of erg s^{-1} cm^{-2}.

Fig. 12.— Miscellaneous single gaussian fits.

Fig. 13.— Miscellaneous multiple gaussian fits.

Fig. 14.— Two gaussian models for the C IV lines from phase 1905.95.

Fig. 15.— Two gaussian models for the Mg II h- and k-lines from phase 1905.96. Note that for simplicity, the IS absorption feature has been approximated by a single gaussian and subtracted from the total flux. For the top panel, the 2797.998 ÅMg II subordinate k-line of the K-star was fixed at the same peak intensity and width as observed at phase 1906.33, where it is unblended from the other lines, but fixed with the predicted stellar radial velocity for phase 1905.96.

Fig. 16.— The difference between the observed Mg II h-profiles and the AT best fit to the ϕ =19065.96 model as a function of phase.

0.53

0.74

0.62

0.81

0.68

0.88

0.72

2802 2803 2804 2805

Wavelength (Å)

2801 2802 2803 2804 2805

Wavelength (Å)

0.61

0.67

0.80

0.87

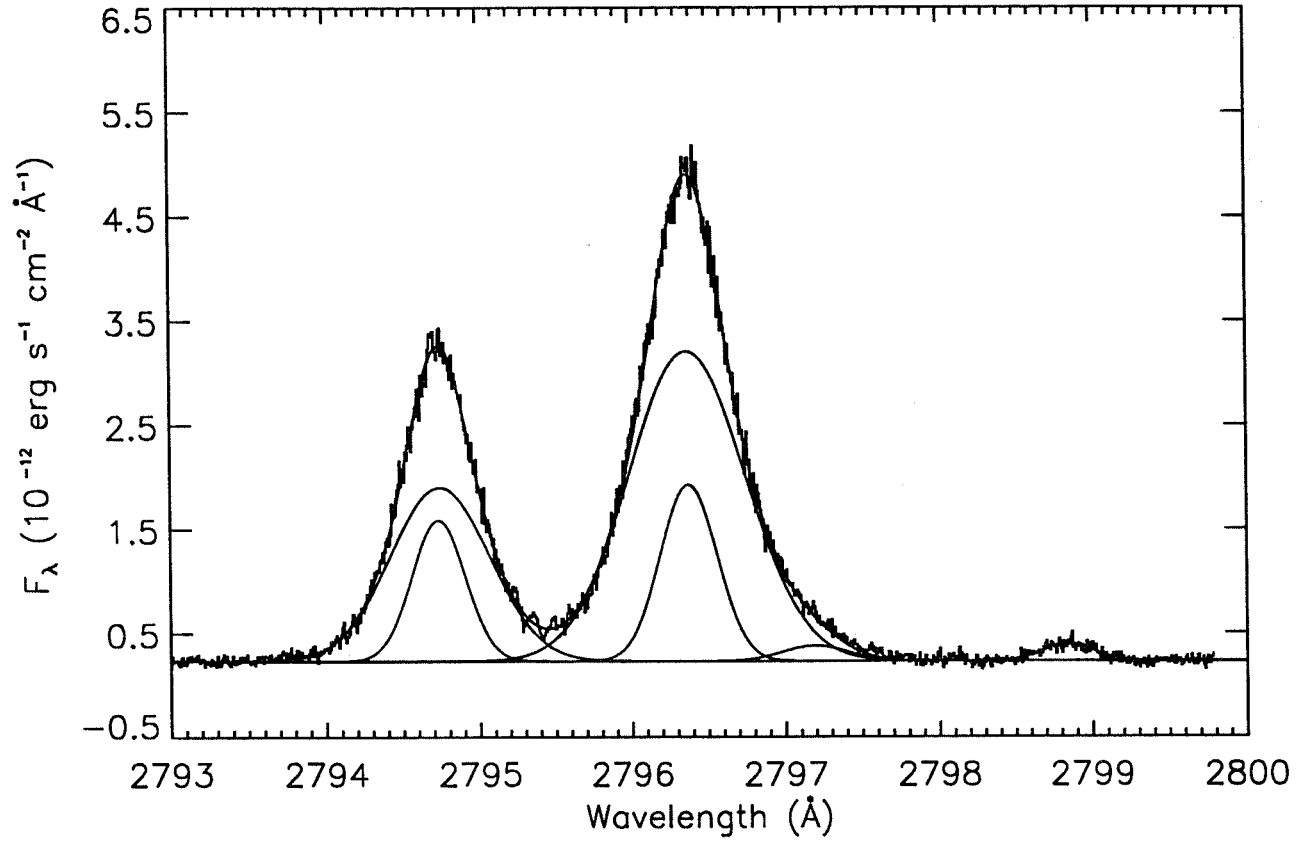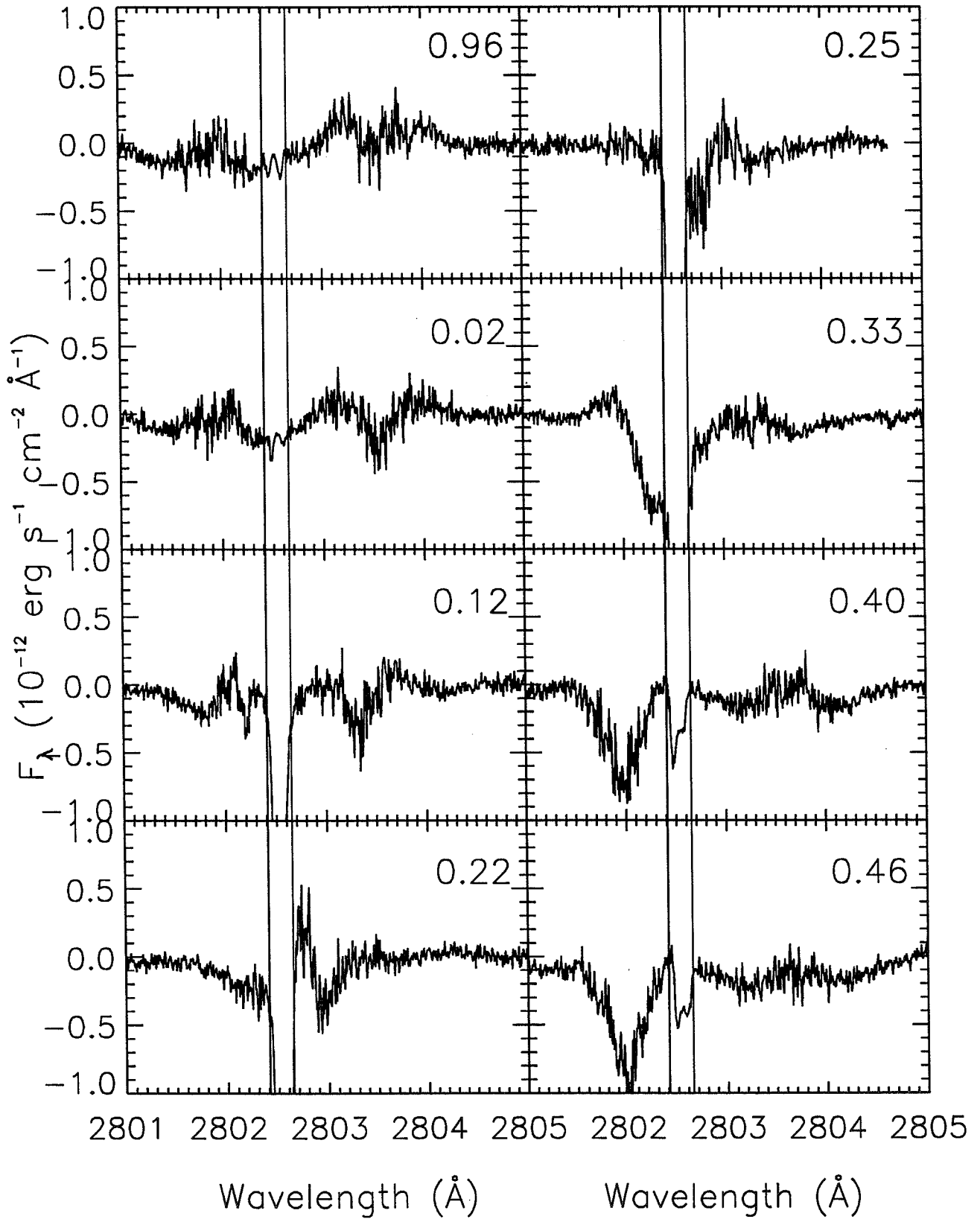1546   1548   1550   1552

Wavelength (Å)

1350 1352 1354 1556 1358

Wavelength (Å)

Wavelength (Å)
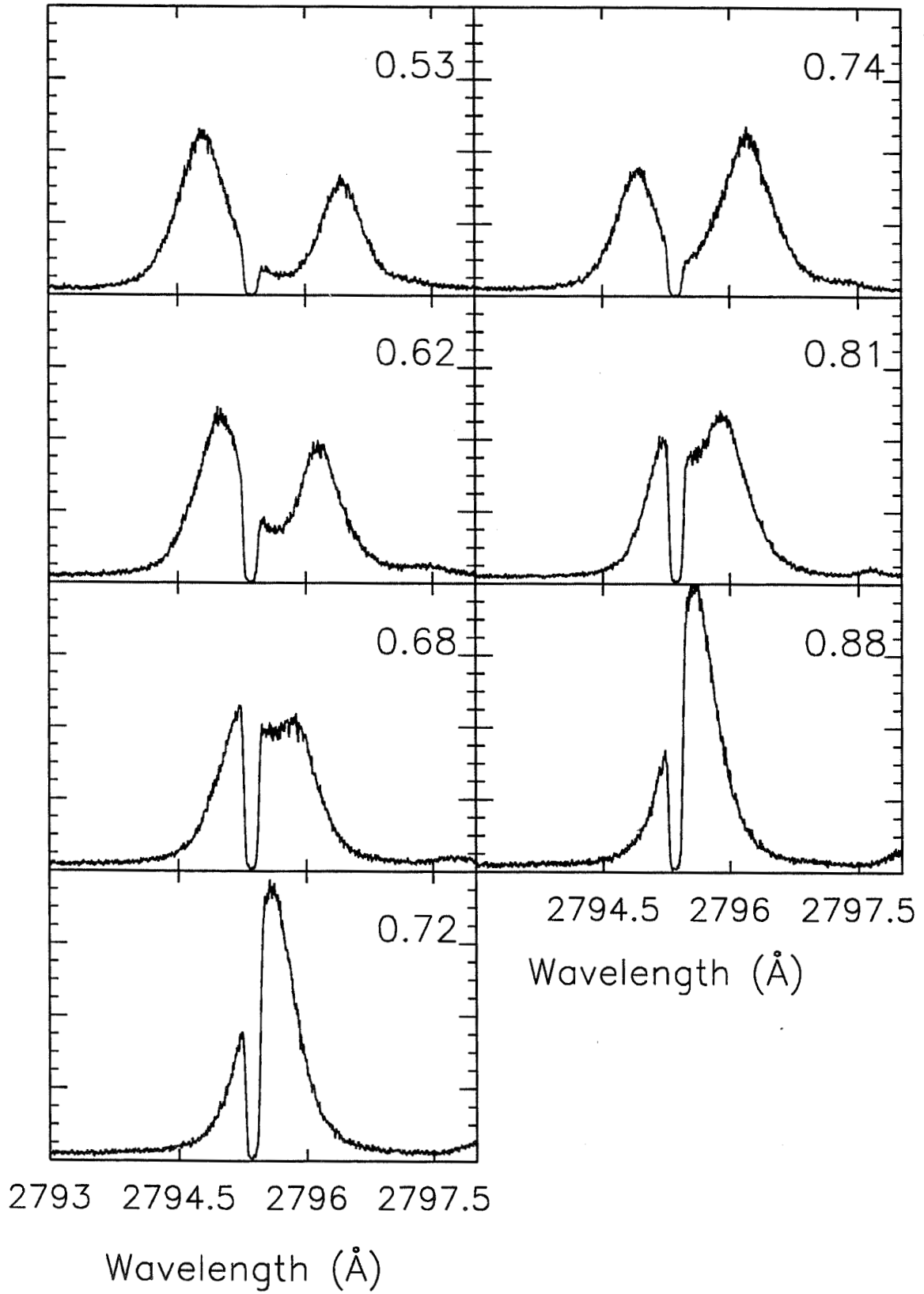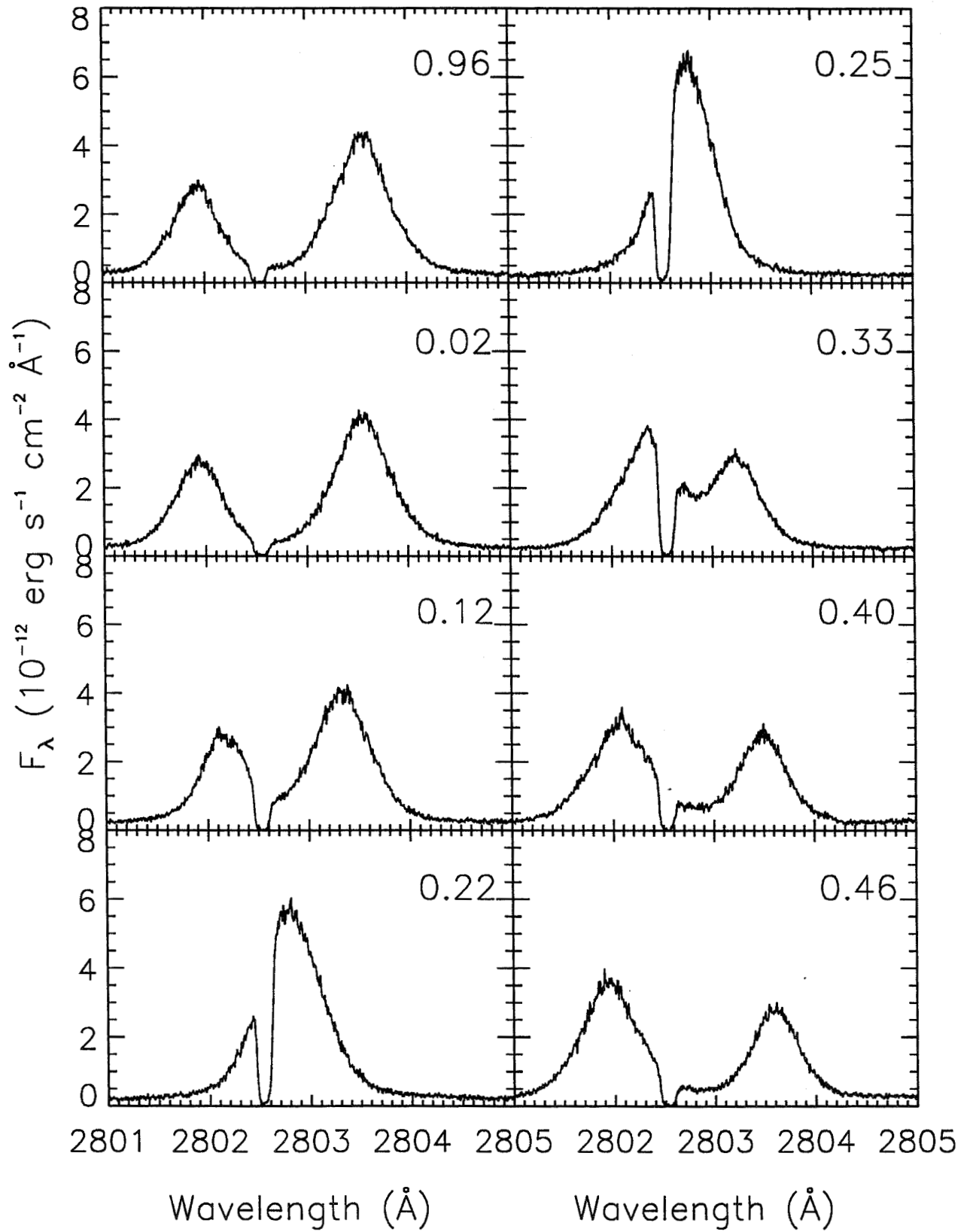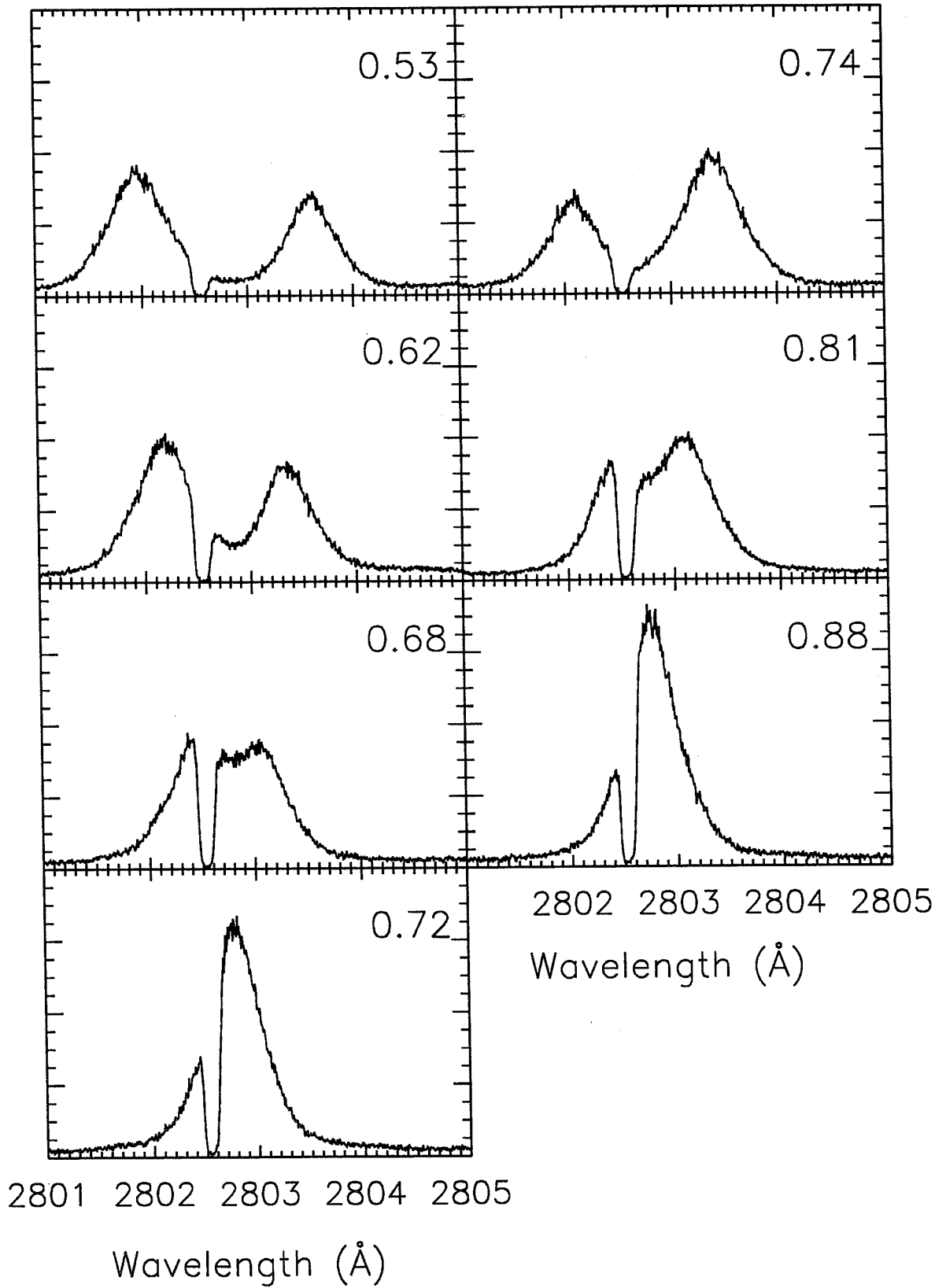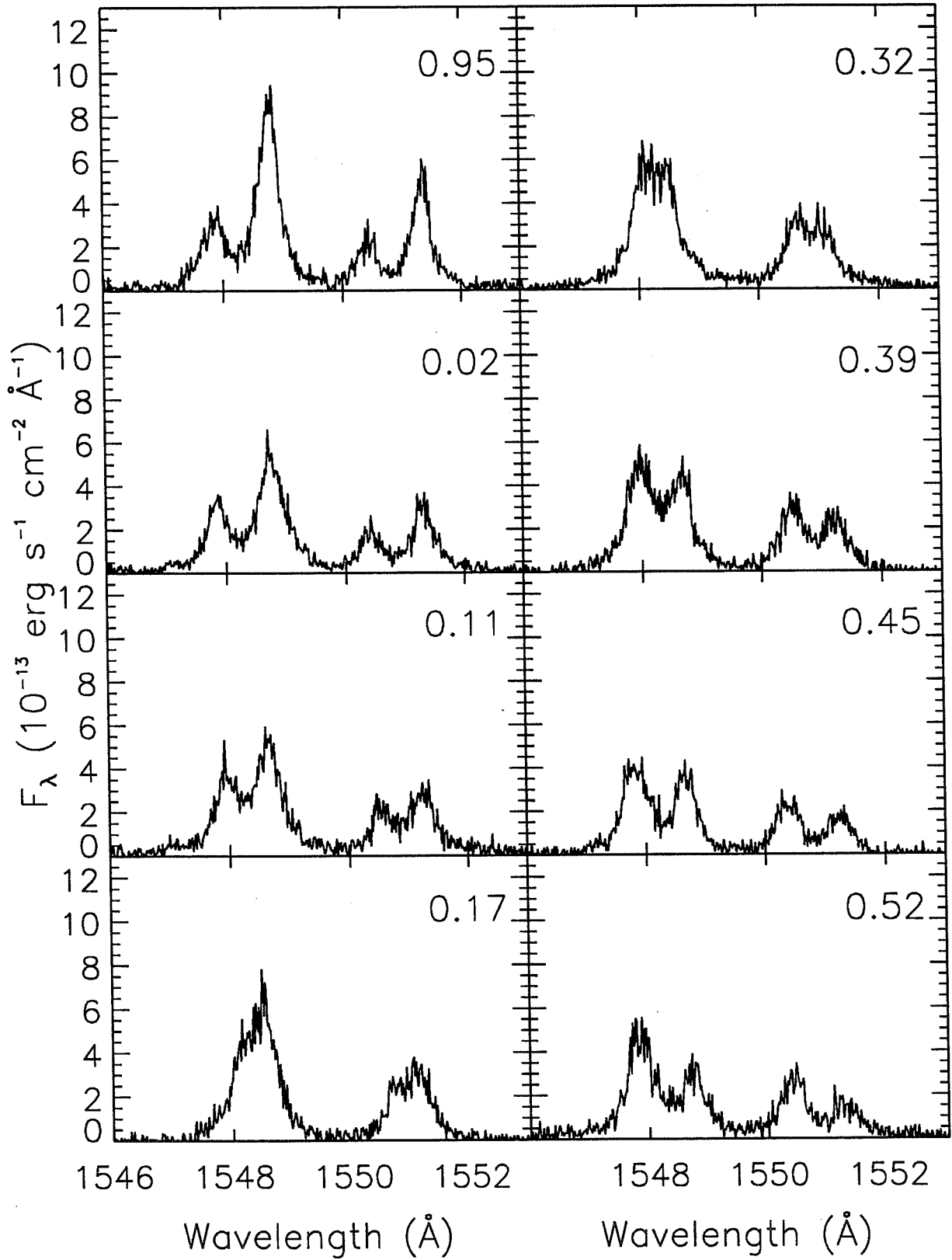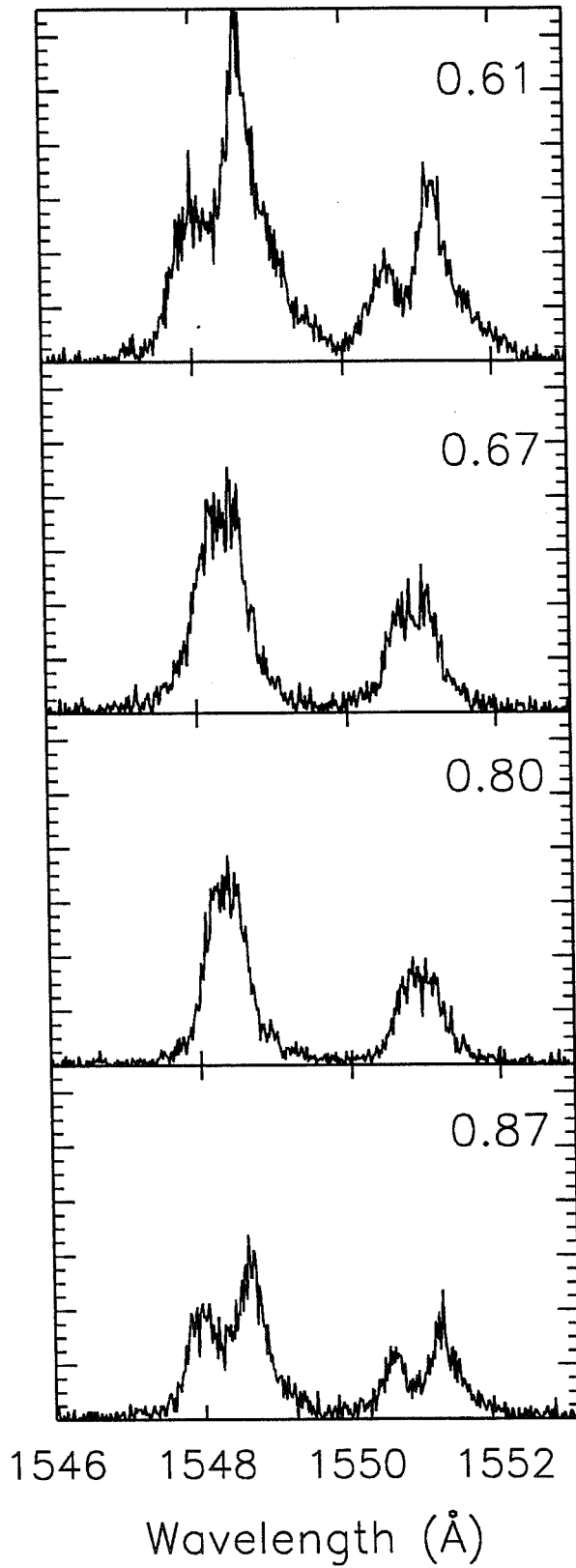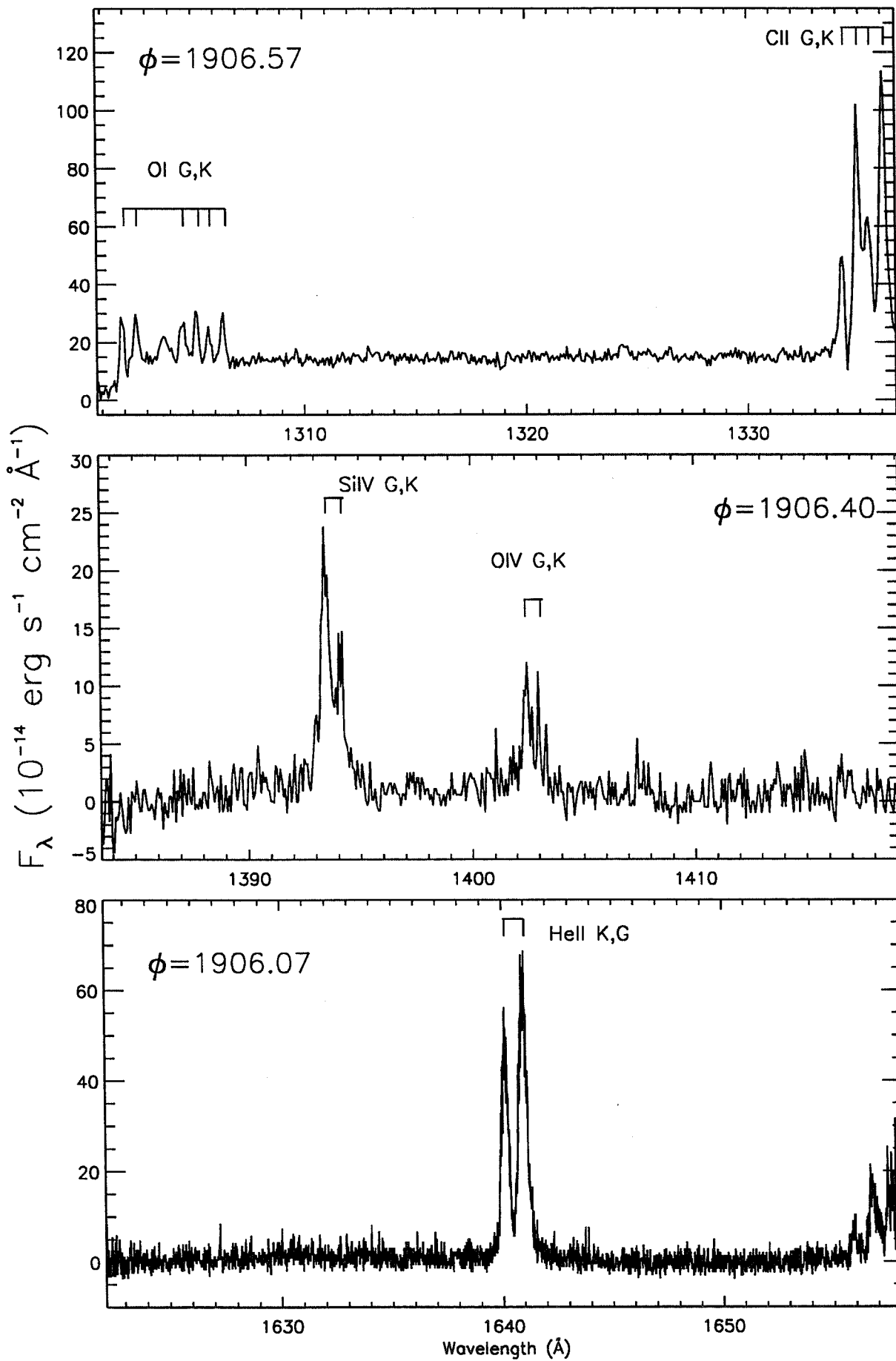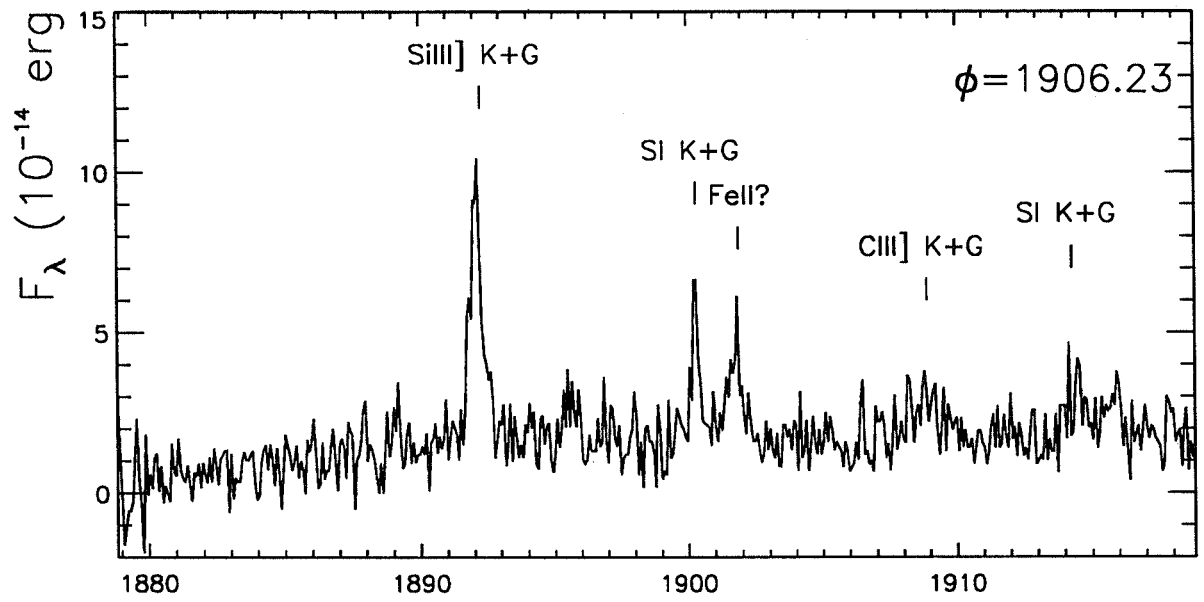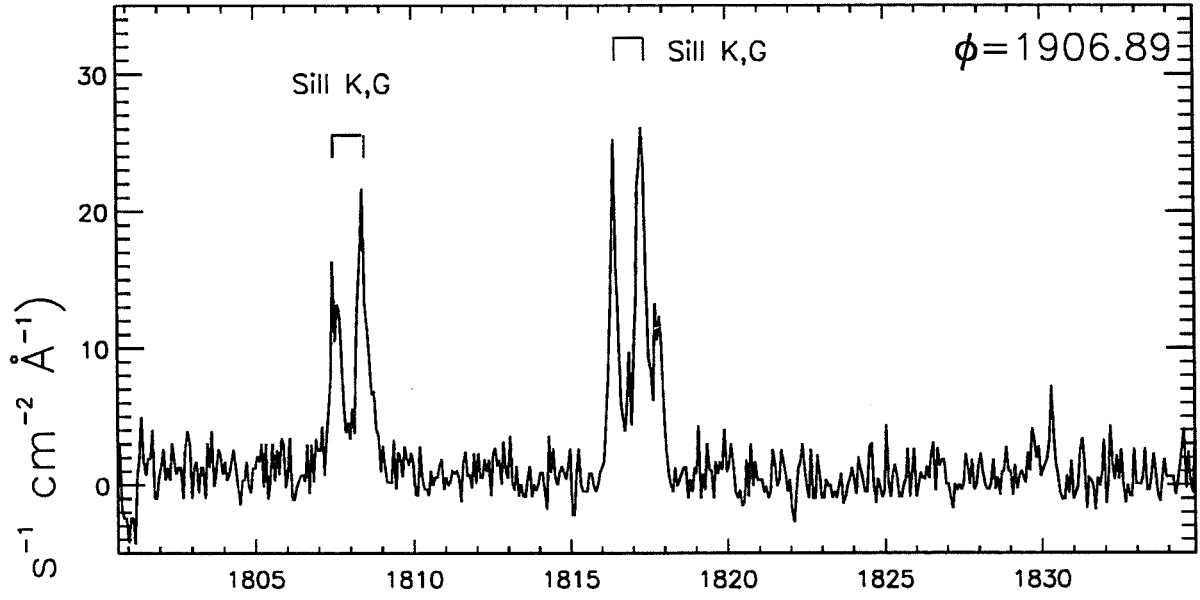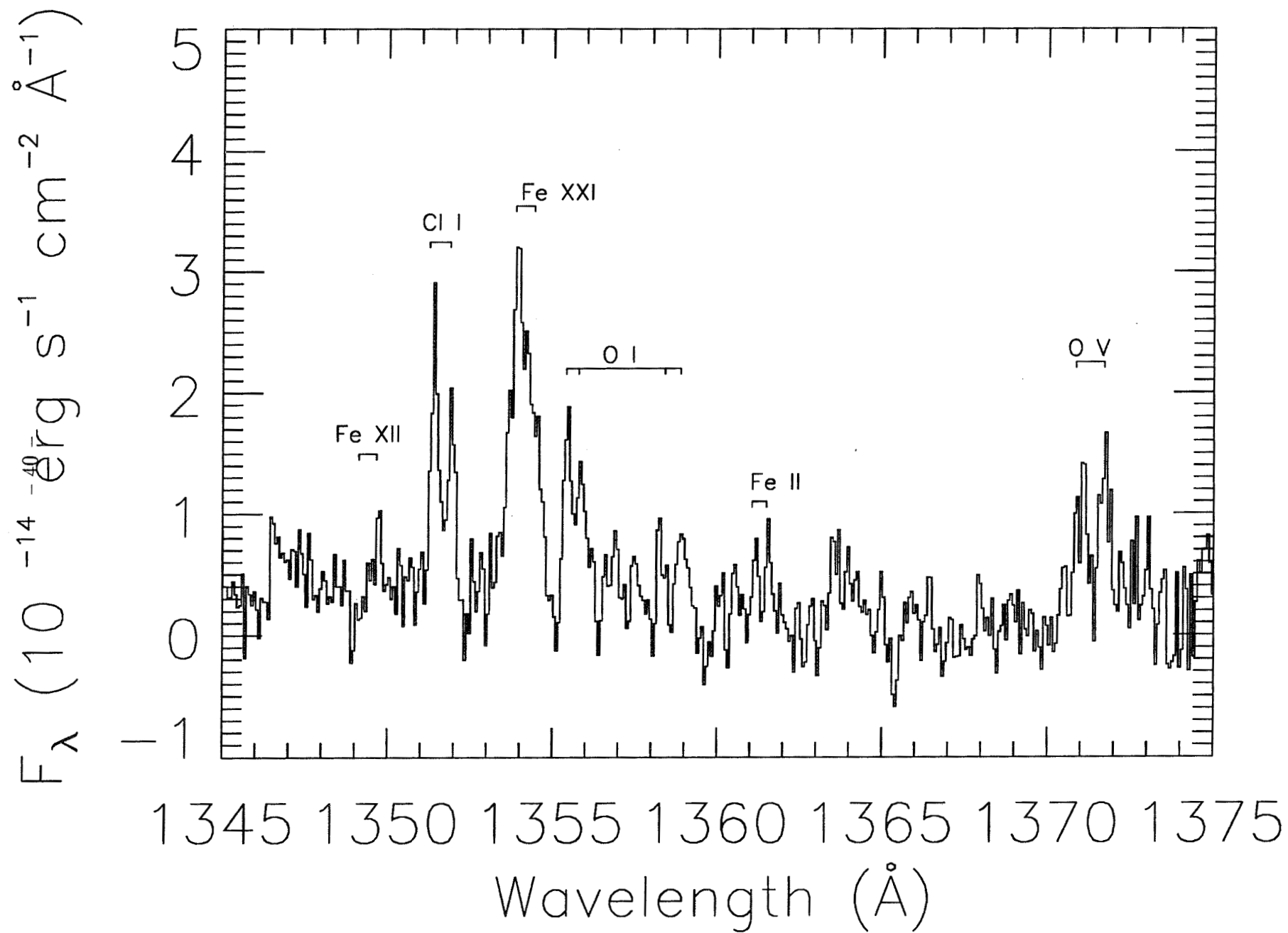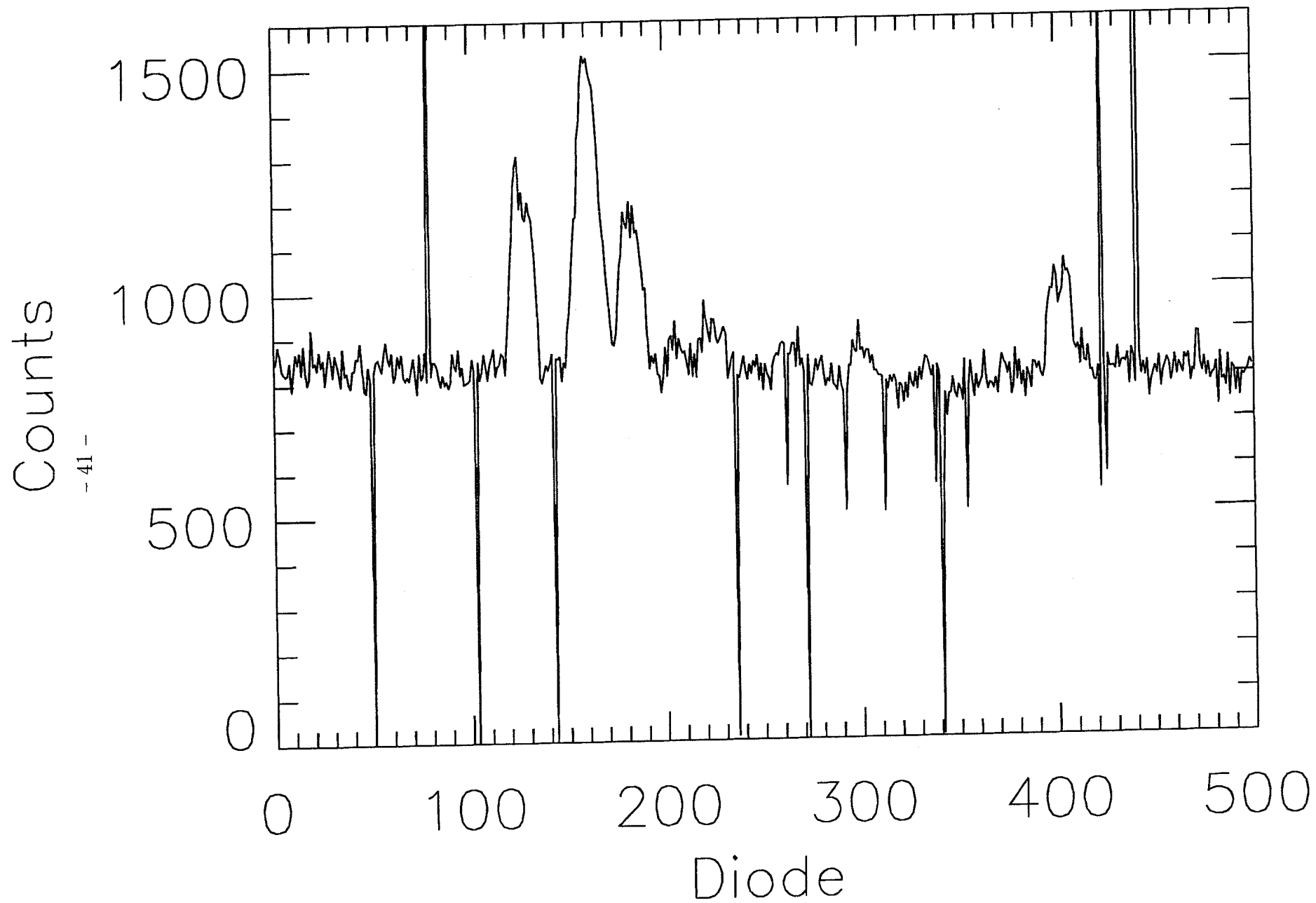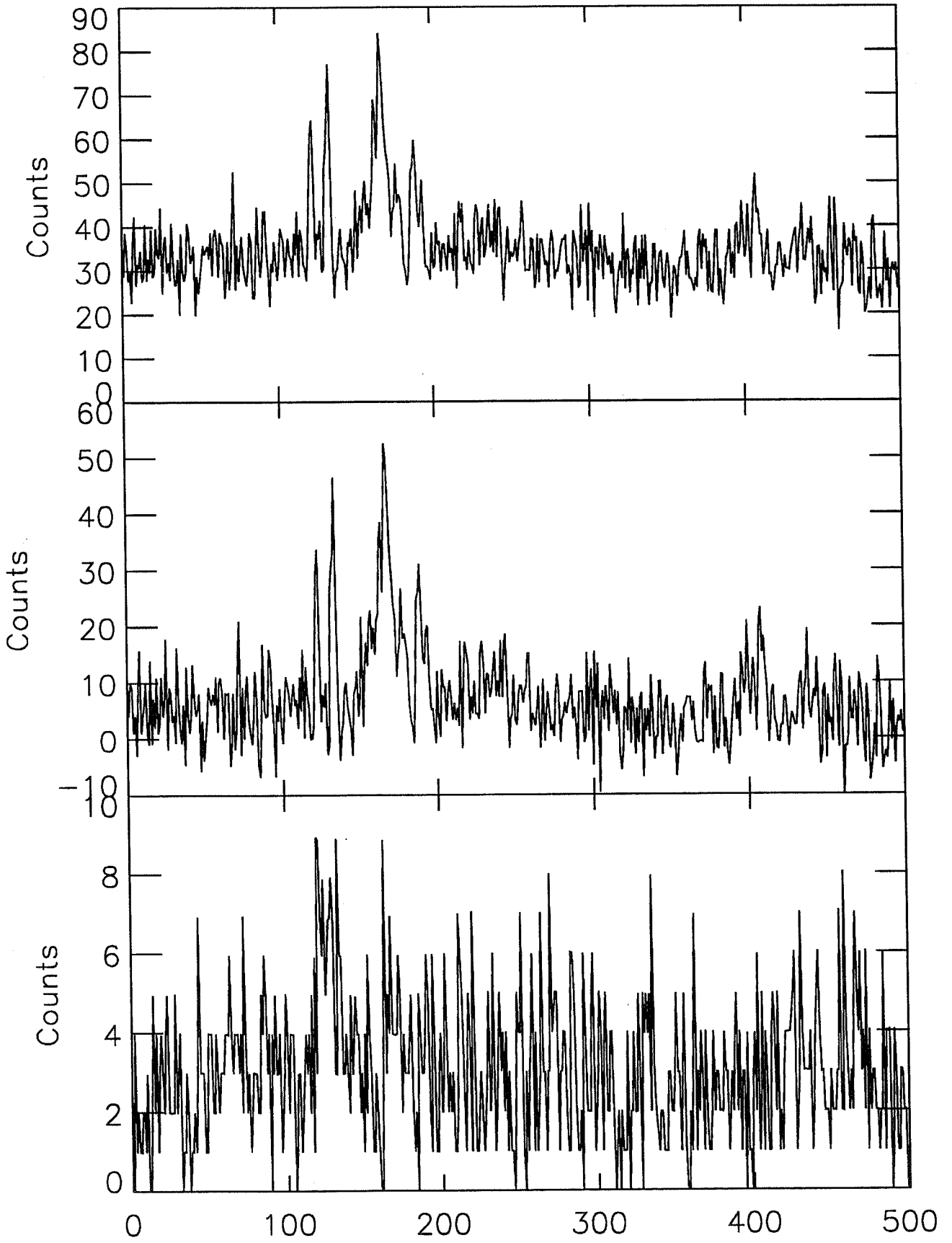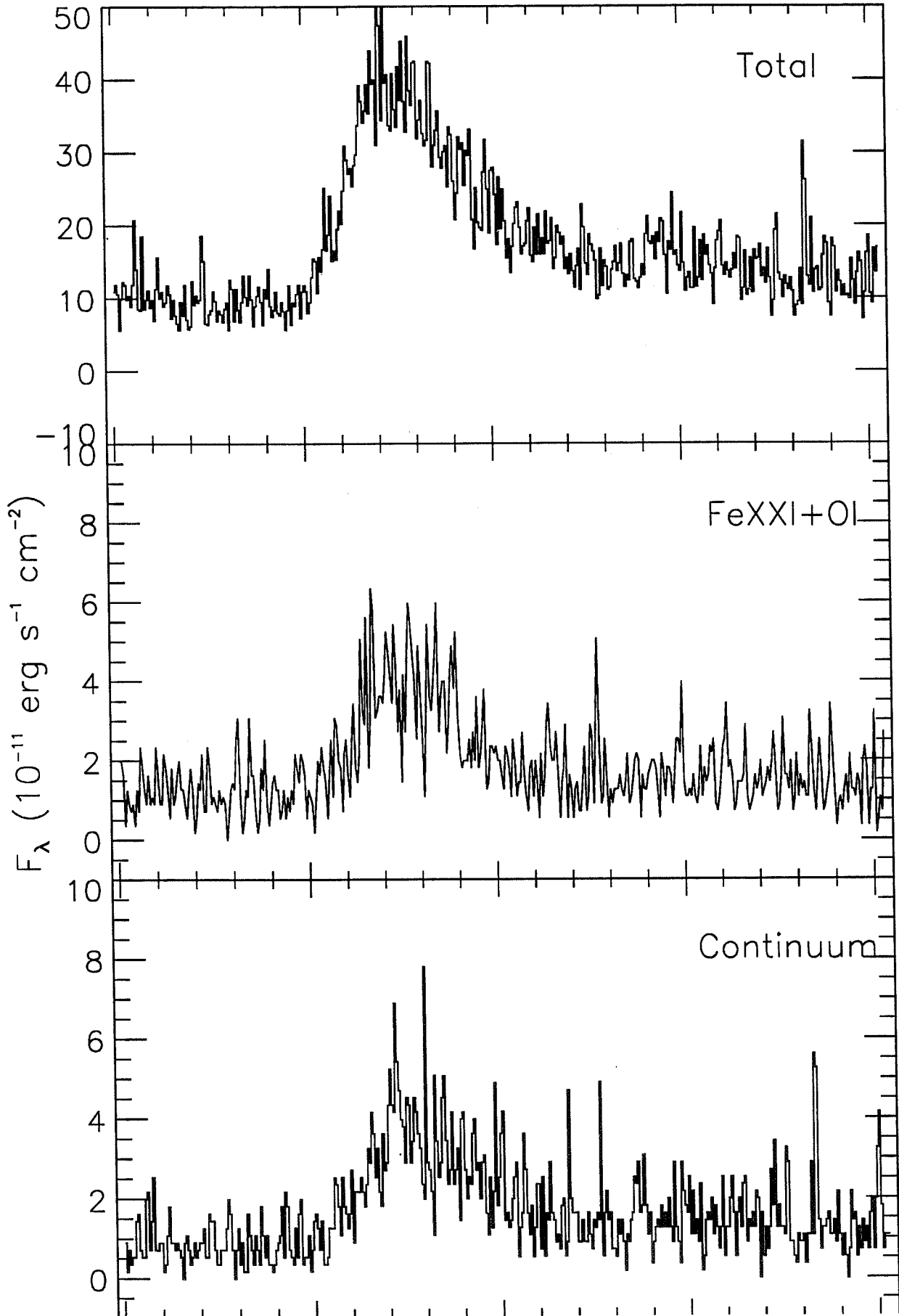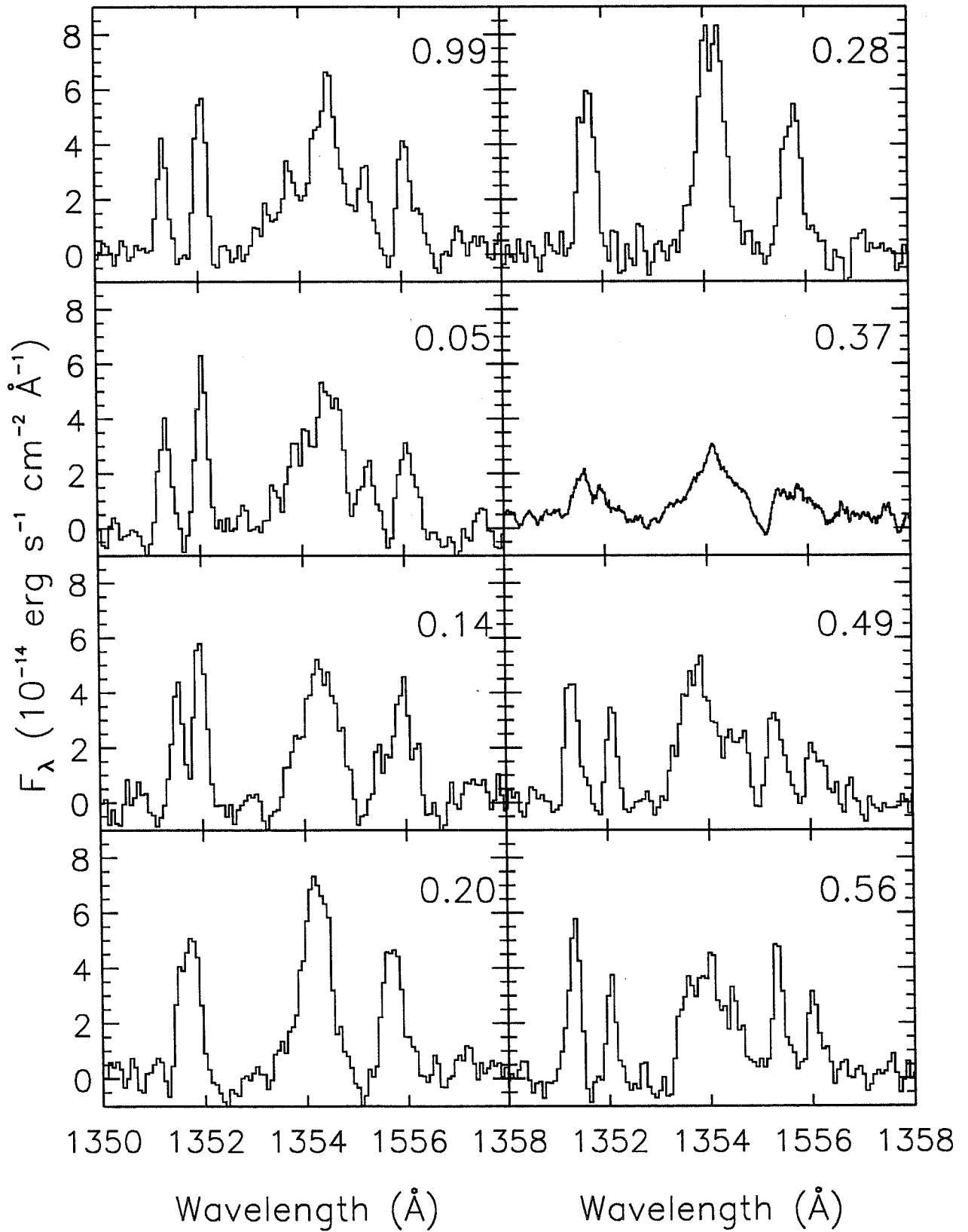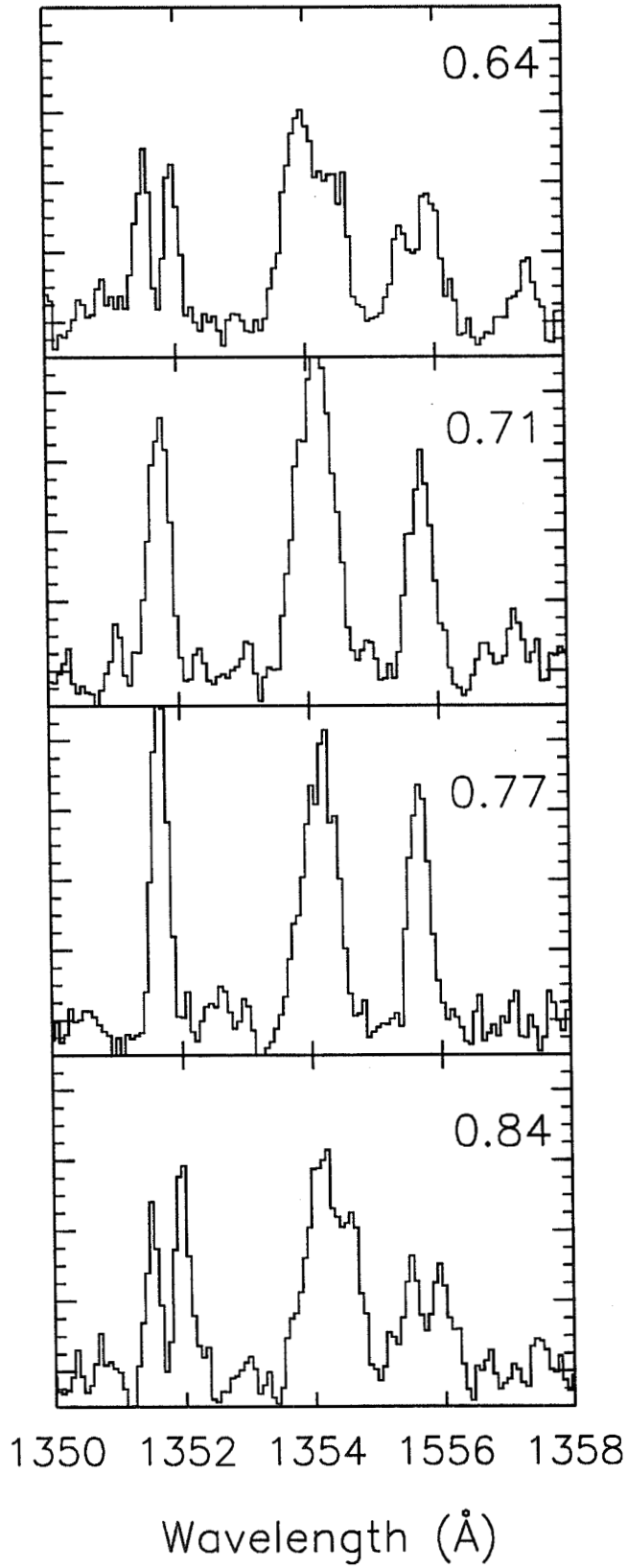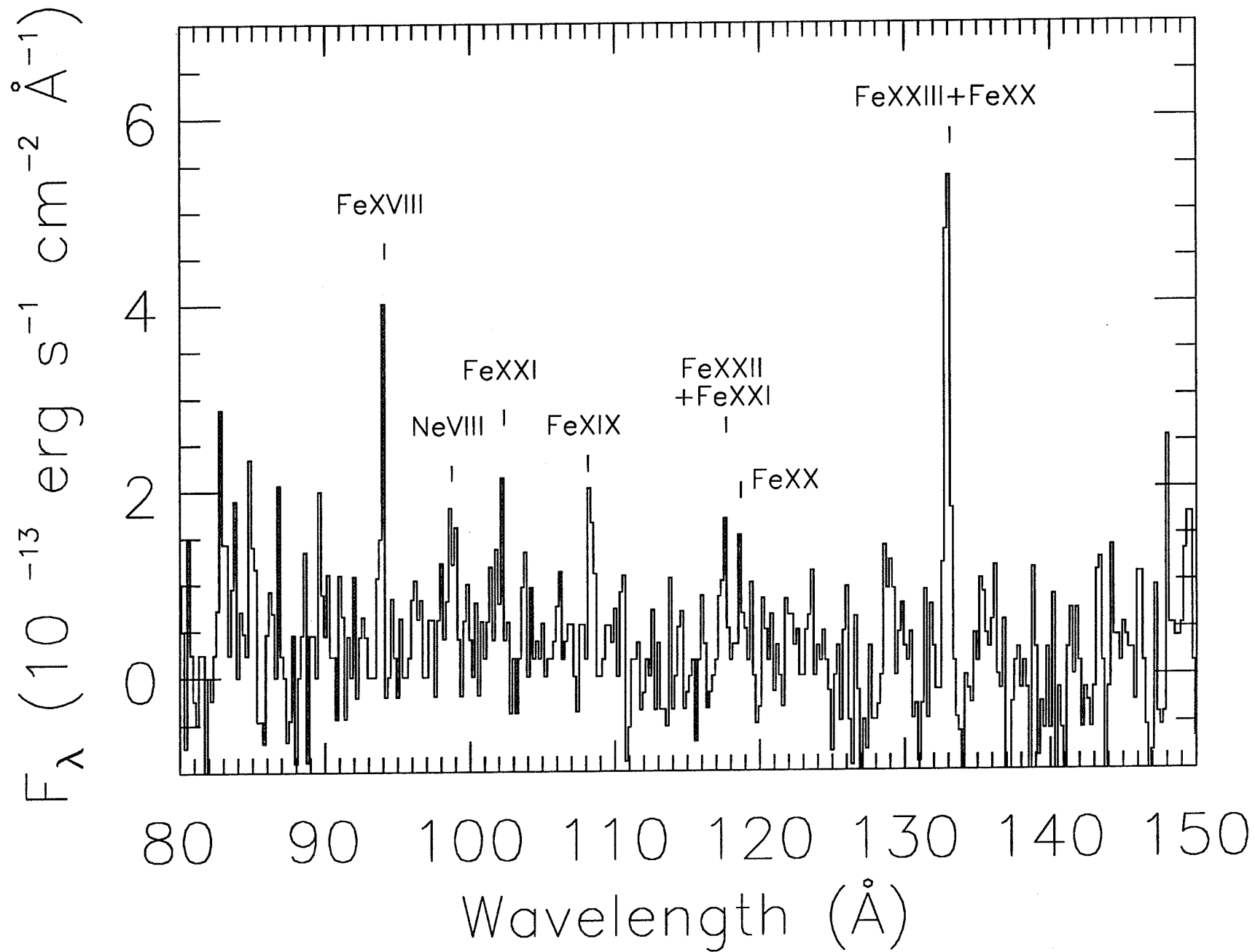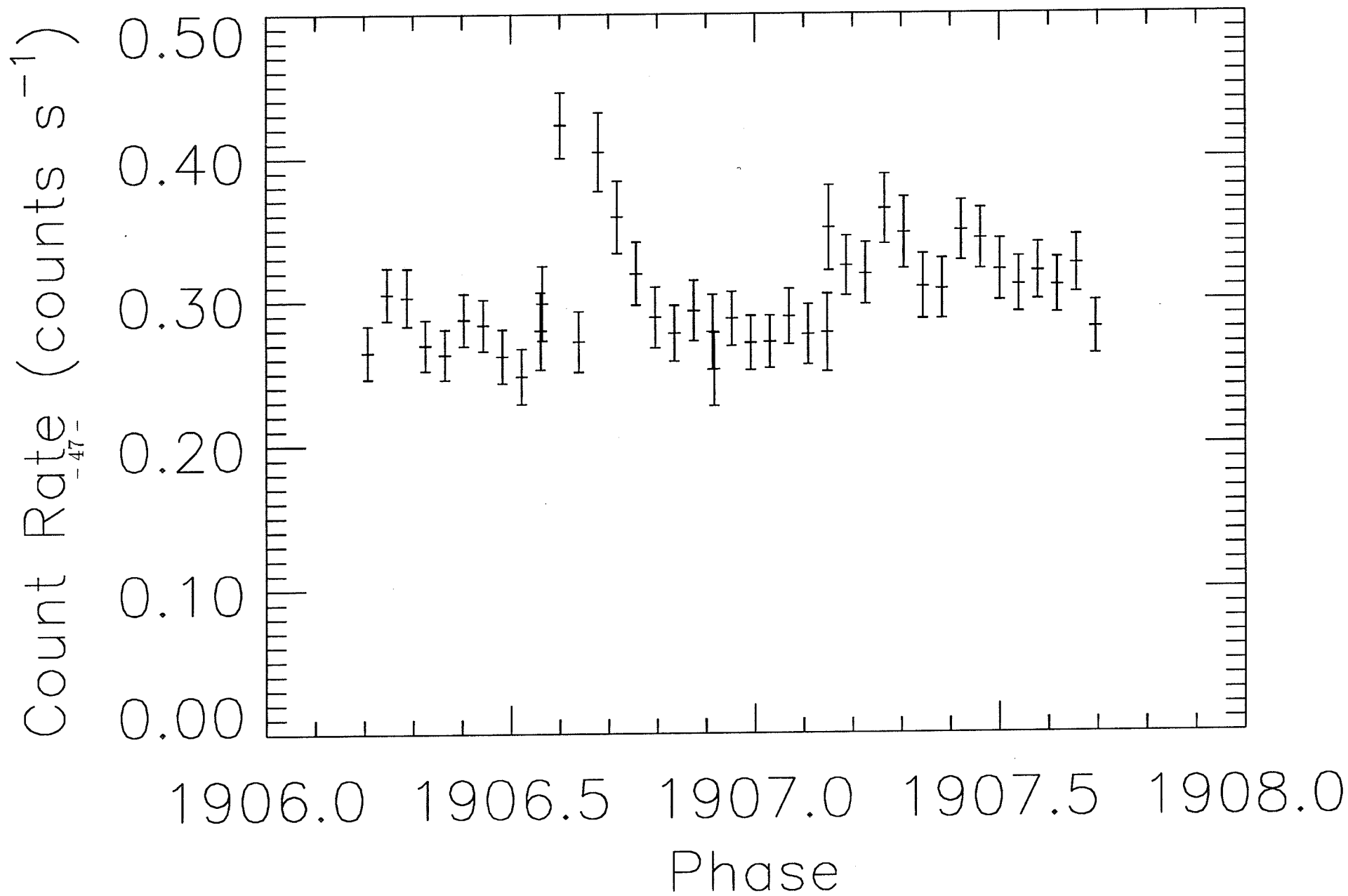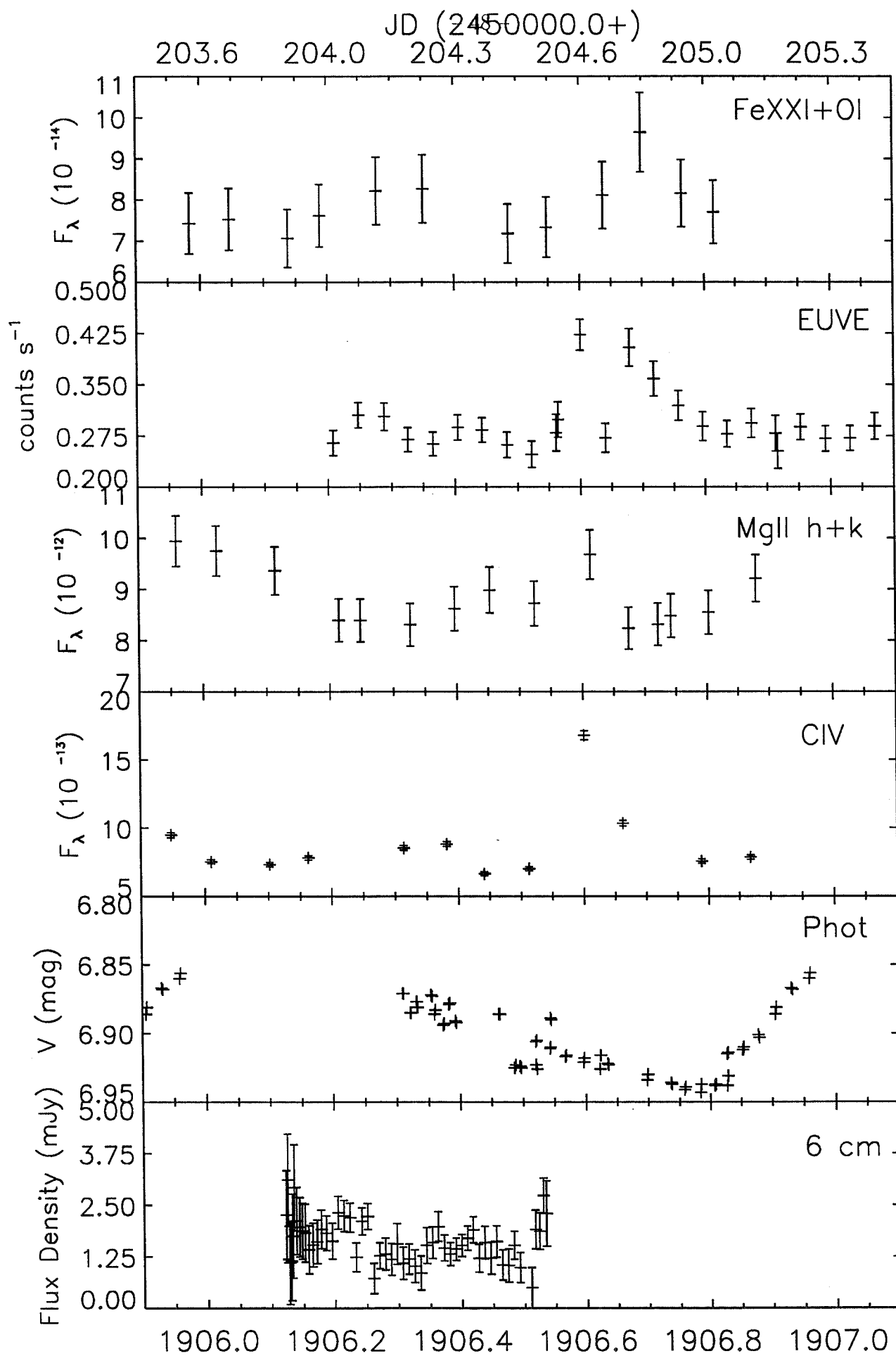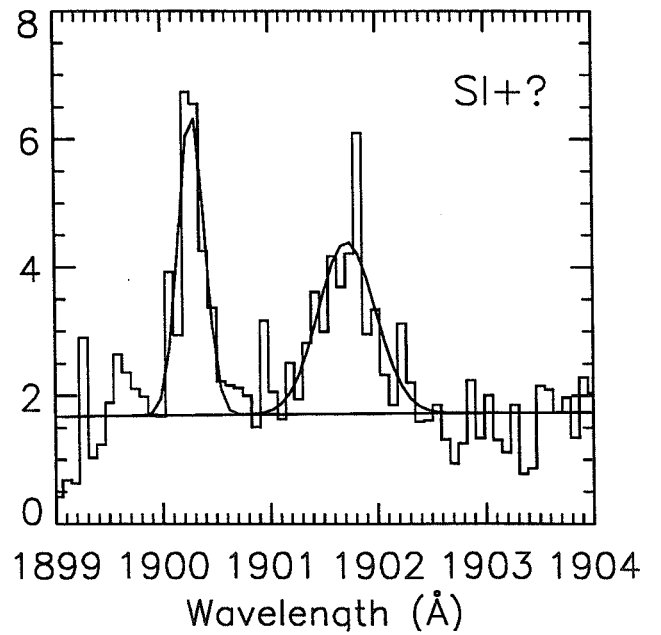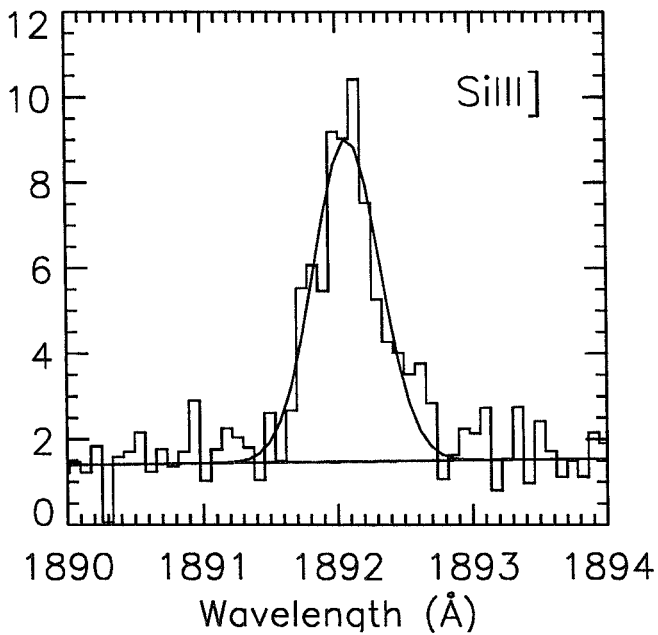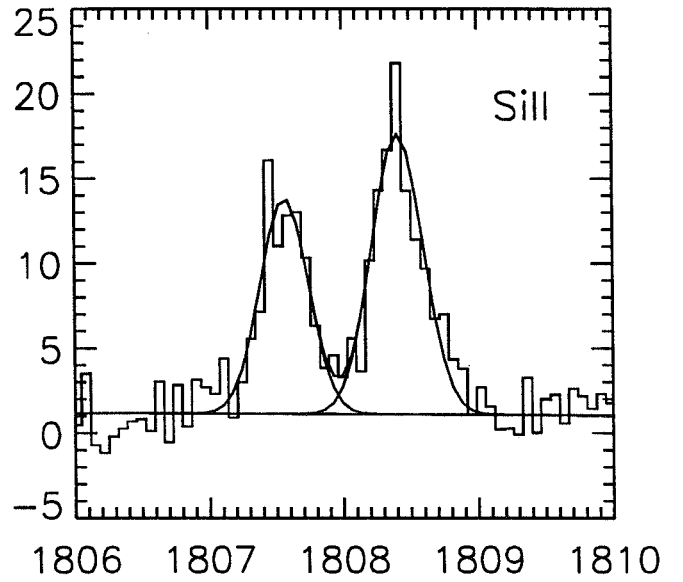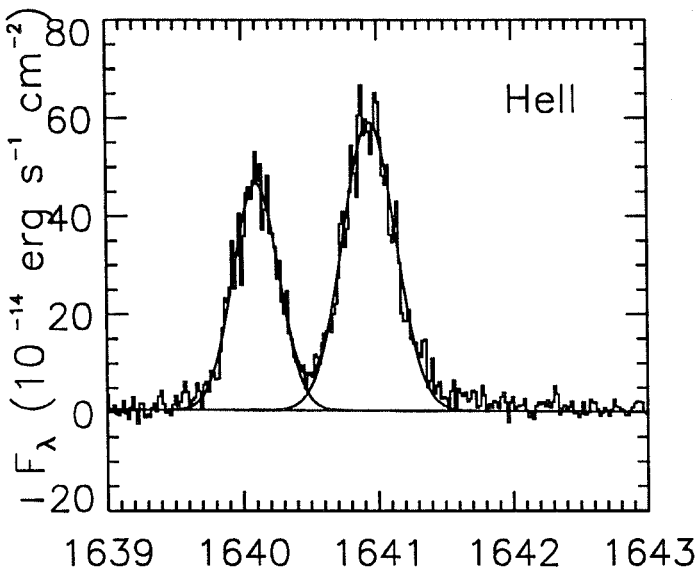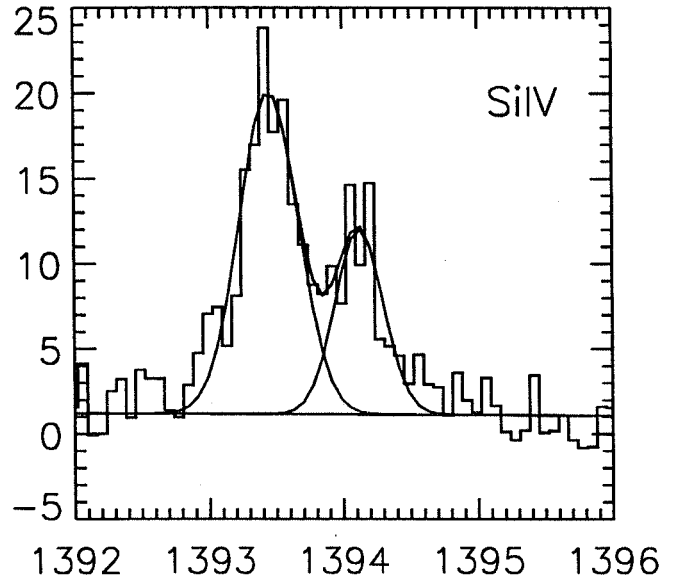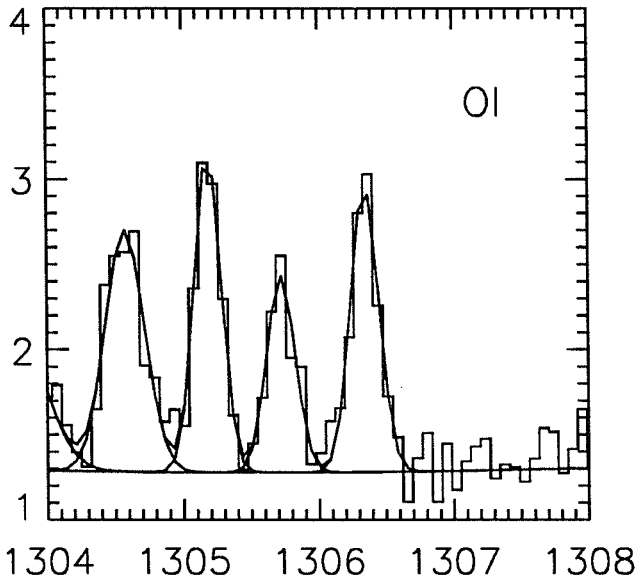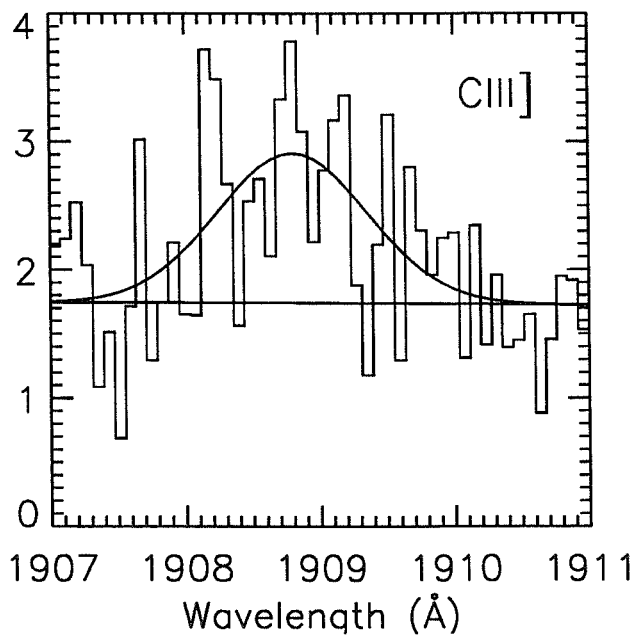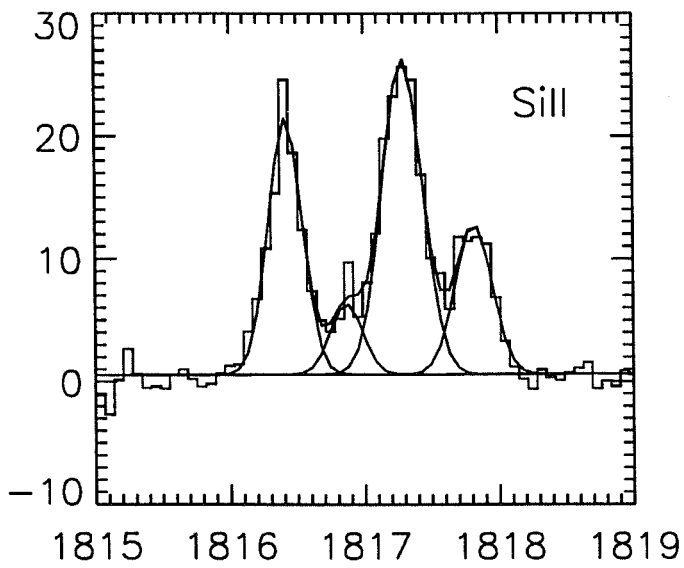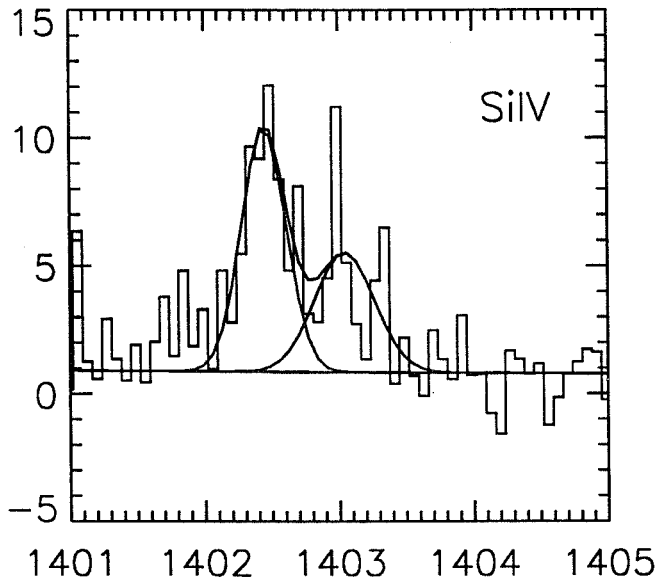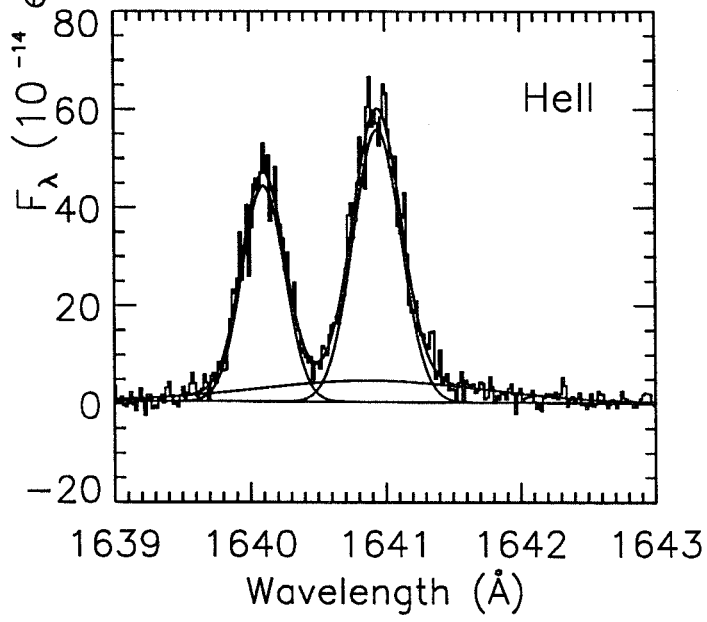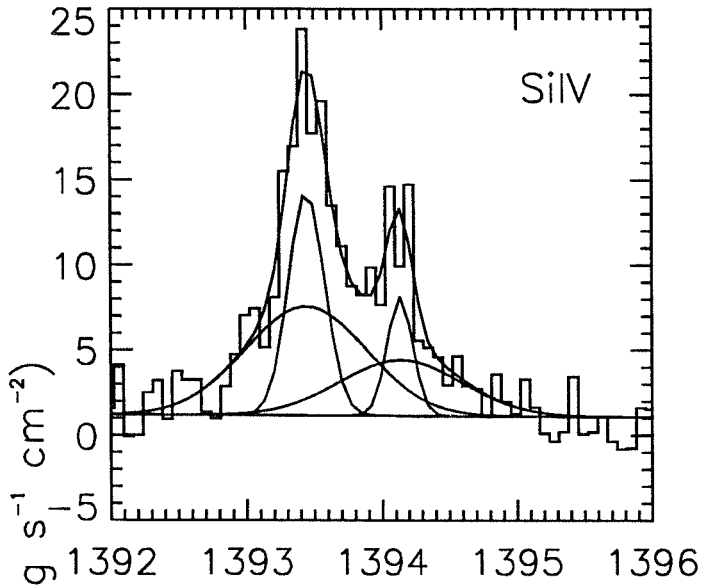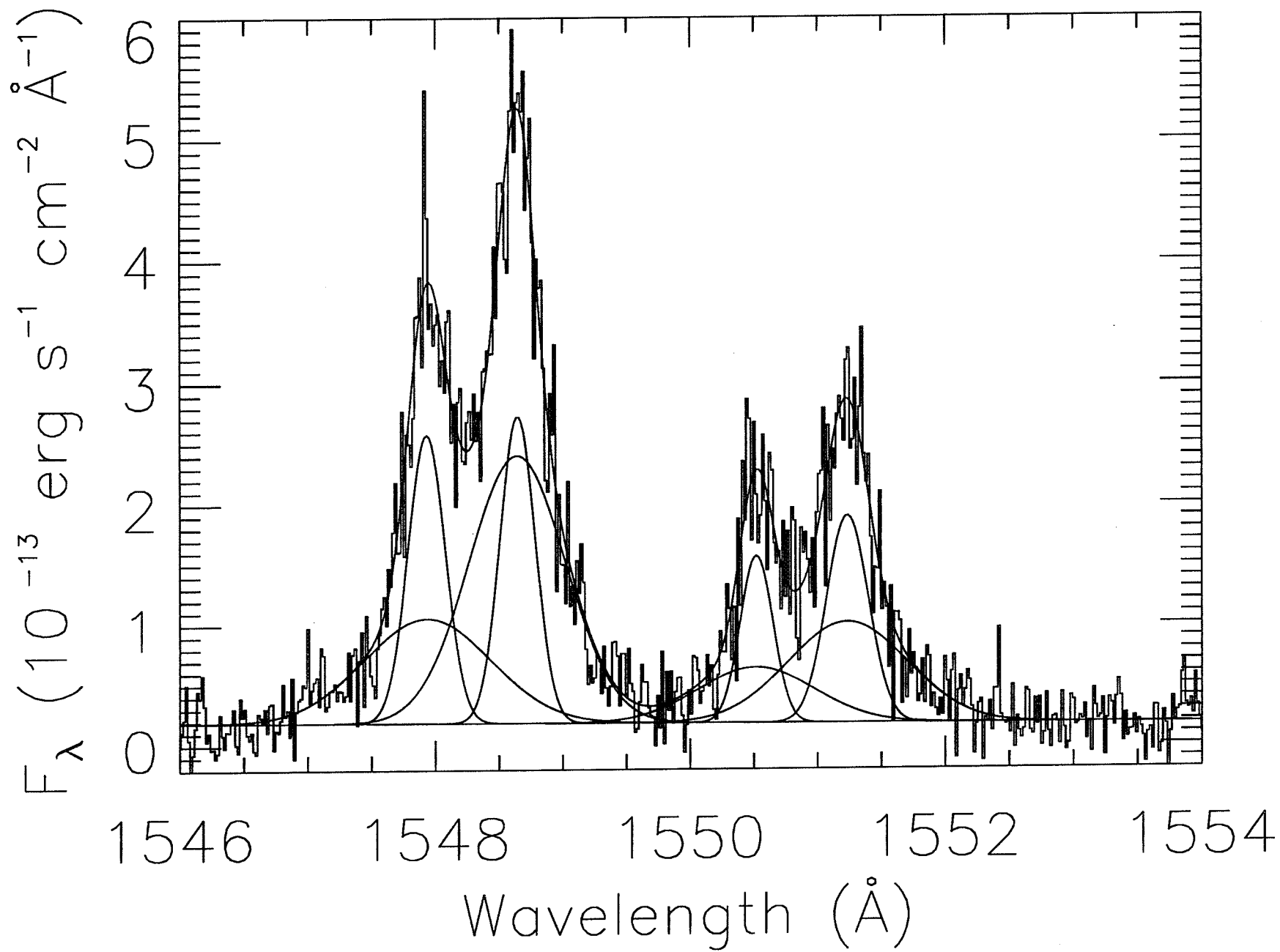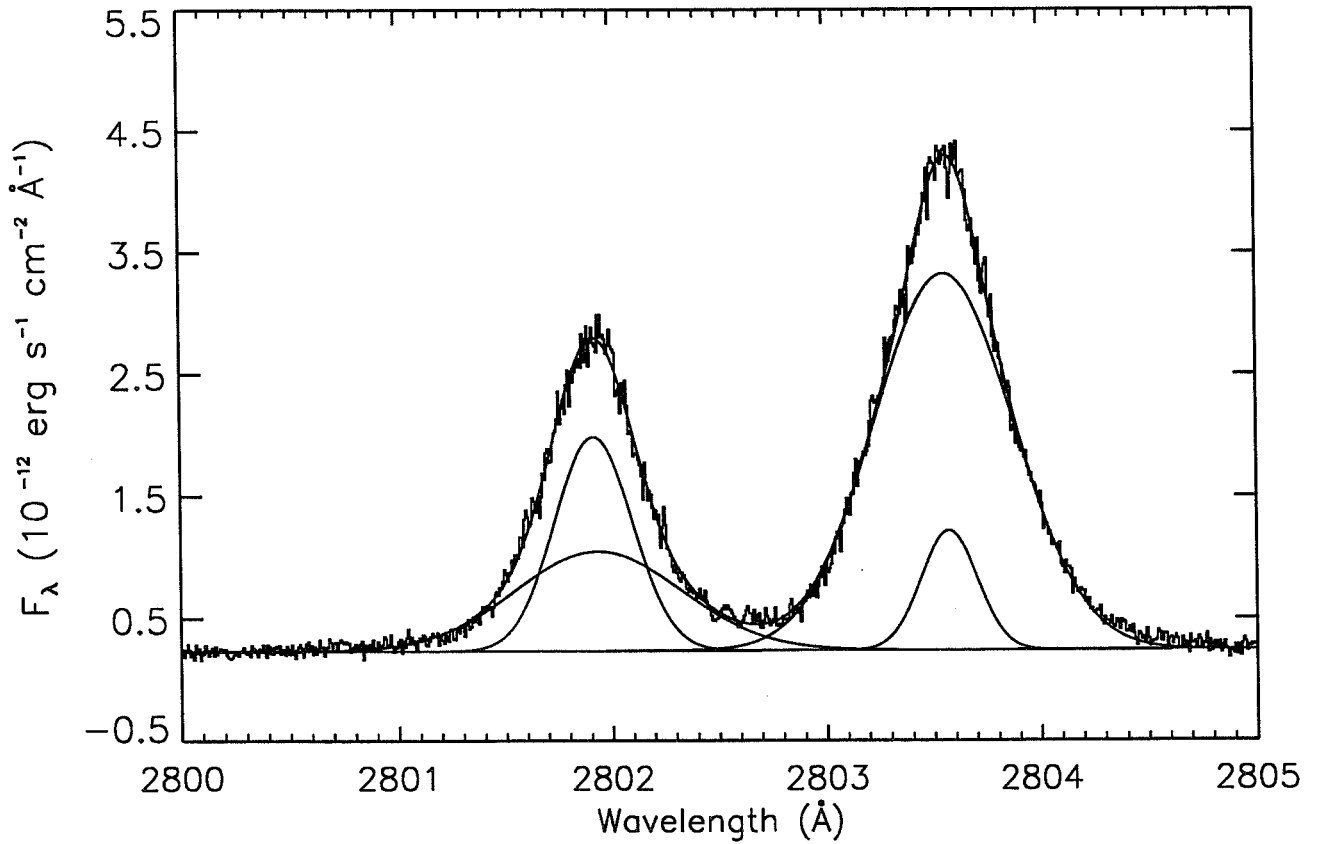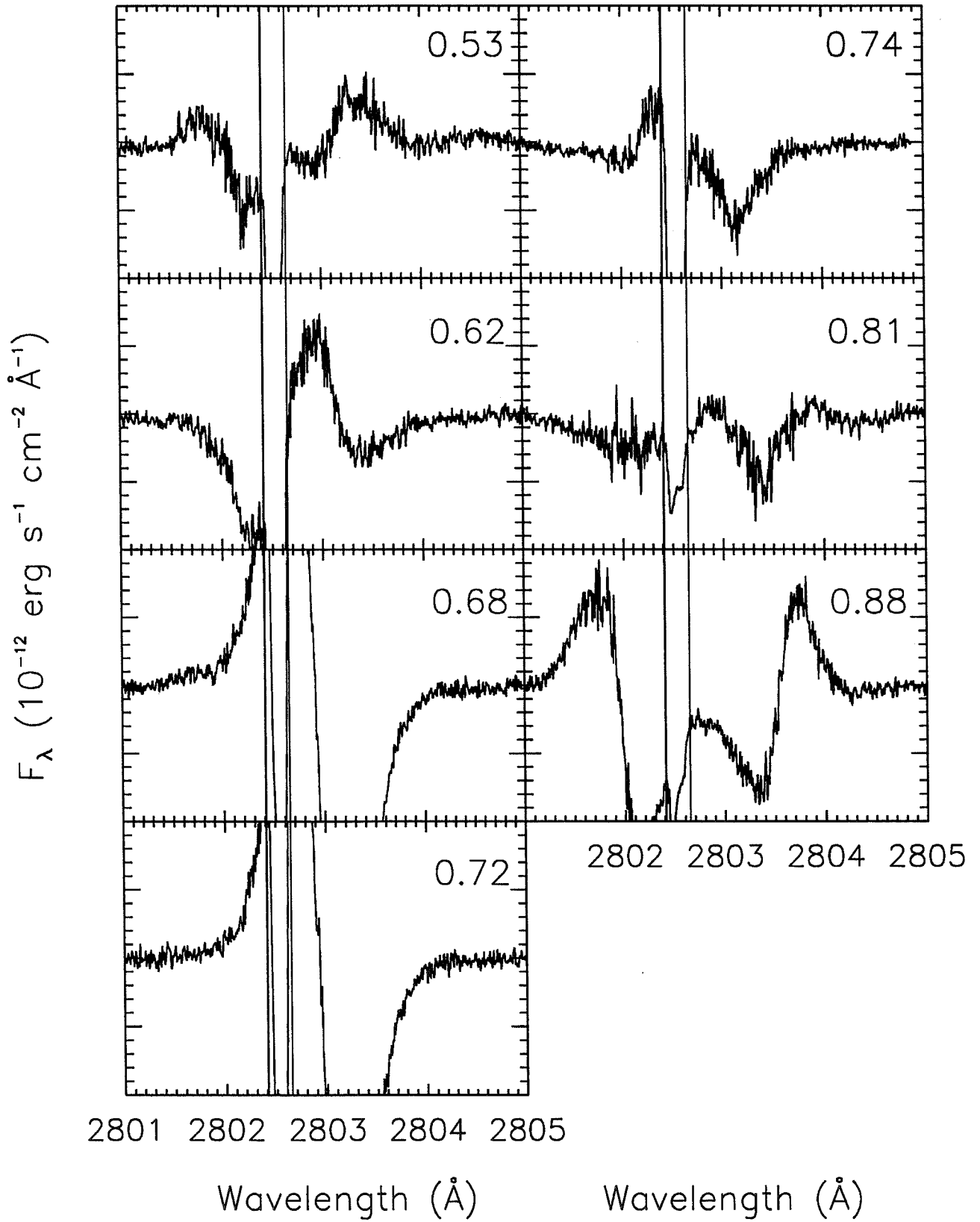
REPORT DOCUMENTATION PAGE

Public reporting burden for this collection of information is estimated to average 1 hour per response, including the time for reviewing instructions, searching existing data sources, gathering and maintaining the data needed, and completing and reviewing the collection of information. Send comments regarding this burden estimate or any other aspect of this collection of information, including suggestions for reducing this burden, to Washington Headquarters Services, Directorate for Information Operations and Reports, 1215 Jefferson Davis Highway, Suite 1204, Arlington, VA 22202-4302, and to the Office of Management and Budget, Paperwork Reduction Project (0704-0188), Washington, DC 20503.

1. AGENCY USE ONLY (Leave blank)	2. REPORT DATE January 1998	3. REPORT TYPE AND DATES COVERED Contractor Report

4. TITLE AND SUBTITLE
NRA–First Multiwavelength, Multiple Layer Doppler Imaging of an Active Binary

5. FUNDING NUMBERS
S-57788-Z

6. AUTHOR(S)
R.C. Dempsey

7. PERFORMING ORGANIZATION NAME(S) AND ADDRESS (ES)
Computer Sciences Corporation
System Sciences Division
1100 West Street
Laurel, MD 20707

8. PEFORMING ORGANIZATION REPORT NUMBER
HMCZ0056

9. SPONSORING / MONITORING AGENCY NAME(S) AND ADDRESS (ES)
National Aeronautics and Space Administration
Washington, DC 20546-0001

10. SPONSORING / MONITORING AGENCY REPORT NUMBER
CR–206874

11. SUPPLEMENTARY NOTES

12a. DISTRIBUTION / AVAILABILITY STATEMENT
Unclassified–Unlimited
Subject Category: 89
Report available from the NASA Center for AeroSpace Information,
7121 Standard Drive, Hanover, MD 21076-1320. (301) 621-0390.

12b. DISTRIBUTION CODE

13. ABSTRACT (Maximum 200 words)

In this final report, grantee reports on data obtained from 26 orbits of continuous observing time with the Hubble Space Telescope's Goddad High Resolution Spectrograph in order to produce a comprehensive 2-D image of the RSCVn V824 Ara at MgII, CIV and for the first time ever, the coronal diagnostic line of FeXXI 1356A.

14. SUBJECT TERMS
HST; EUVE; plasma; photosphere; chromosphere; corona; flares.

15. NUMBER OF PAGES
55

16. PRICE CODE

17. SECURITY CLASSIFICATION OF REPORT	18. SECURITY CLASSIFICATION OF THIS PAGE	19. SECURITY CLASSIFICATION OF ABSTRACT	20. LIMITATION OF ABSTRACT
Unclassified	Unclassified	Unclassified	UL